Investigation of Drop Size Distributions recorded by a Network of Disdrometers during the Swabian MOSES Campaign 2021

Master's Thesis in Meteorology
by

Sören Bergmann

April 2022

Karlsruher Institut für Technologie

INSTITUTE OF METEOROLOGY AND CLIMATE RESEARCH
KARLSRUHE INSTITUTE OF TECHNOLOGY (KIT)

Advisor:	Prof. Dr. Michael Kunz
Second Advisor:	Prof. Dr. Corinna Hoose

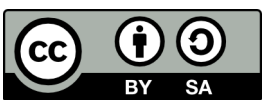

Abstract

This study investigates drop size distributions (DSDs) and precipitation properties of rain events in the Neckar Valley and the Swabian Jura in southwestern Germany. The gamma distribution and the moments method are utilised to describe and deduce DSD parameters from data recorded by a laser optical disdrometer network of 23 Parsivels, deployed in the framework of the Swabian MOSES field campaign conducted in summer 2021.
A quality control is developed for this network used for the first time. To test the accuracy of the disdrometers a comparison of data measured by collocated Parsivels is done. For the median volume diameter D_0, it is shown that variations can be attributed to the expected statistical variations of this parameter.
The mutual dependencies of the gamma distribution parameters as well as their relation with the rain rate are examined by evaluating their two-dimensional frequency distributions. The median volume diameter is found to increase with increasing rain rate up to rain events with $R \approx 40\,\mathrm{mm\,h^{-1}}$ to a maximum of $D_0 = 2.4\,\mathrm{mm}$. Stronger rainfall events exhibit median volume diameter means within a small value range between 2.2 and 2.4 mm. Further, a nearly linear relationship is observed between the shape parameter μ and the slope parameter λ. The normalised intercept parameter N_L exhibits a slight dependence on μ and is relatively constant for different rain rates.
An analysis of the spatial variability of the DSDs reveals the influence that the orographic features of the region have on the parameters. DSDs of rainfall in the Swabian Jura display a distinctively smaller median volume diameter compared to the Neckar Valley while simultaneously exhibiting higher rainfall totals. However, the rainfall total of events with rain rates larger than $20\,\mathrm{mm\,h^{-1}}$ is bigger in the Neckar Valley, which implies a more frequent occurrence of heavy rainfall events.
A time series of the rain intensity, recorded in-situ by the Parsivels, is compared to the observations from an X-band radar, for the supercell that occurred on June 23, 2021. As expected, the coincidence in time between the in-situ measurement and remote sensing is confirmed. Further, the time series of the rain rate and the median volume diameter during the passage of the supercell over Rottenburg display a strong intra-event temporal variability.

Zusammenfassung

In dieser Studie werden Tropfengrößenverteilungen (DSDs) und Niederschlagseigenschaften von Regenereignissen im Neckartal und auf der Schwäbischen Alb in Südwestdeutschland untersucht. Die Gamma-Verteilung und die Momentenmethode werden zur Beschreibung und Ableitung von DSD-Parametern aus den Daten verwendet, die von einem Disdrometer-Netzwerk bestehend aus 23 Parsivels aufgezeichnet wurden. Dieses wurde im Rahmen der Feldkampagne Swabian MOSES im Sommer 2021 eingesetzt.
Zunächst wird eine Qualitätskontrolle für dieses Netzwerk entwickelt, das zum ersten Mal eingesetzt wird. Um die Genauigkeit der Disdrometer zu testen, wird ein Vergleich der von benachbarten Parsivels gemessenen Daten durchgeführt. Für den Tropfendurchmesser mittleren Volumens D_0 wird gezeigt, dass Abweichungen auf die erwarteten statistischen Schwankungen dieses Parameters zurückgeführt werden können.
Die gegenseitigen Abhängigkeiten der Parameter der Gammaverteilung sowie ihr Zusammenhang mit der Regenrate werden durch Auswertung ihrer zweidimensionalen Häufigkeitsverteilungen untersucht. Es zeigt sich, dass der typische Tropfendurchmesser mit zunehmender Regenrate bis zu Regenereignissen mit $R \approx 40\,\mathrm{mm\,h^{-1}}$ auf ein Maximum von $D_0 = 2,4\,\mathrm{mm}$ ansteigt. Stärkere Regenereignisse weisen Mittelwerte des typischen Tropfendurchmessers innerhalb eines kleinen Wertebereichs zwischen 2,2 und 2,4 mm auf. Außerdem wird ein nahezu linearer Zusammenhang zwischen dem Formparameter μ und dem Steigungsparameter λ beobachtet. Der normierte Achsenabschnittsparameter N_L weist eine leichte Abhängigkeit von μ auf und ist für verschiedene Regenraten relativ konstant.
Eine Analyse der räumlichen Variabilität der DSDs zeigt den Einfluss der Orographie des Messgebiets auf die Parameter. DSDs von Niederschlägen auf der Schwäbischen Alb weisen im Vergleich zum Neckartal einen deutlich kleineren typischen Tropfendurchmesser bei gleichzeitig höheren Niederschlagssummen auf. Allerdings ist die Niederschlagssumme von Ereignissen mit Regenraten größer als $20\,\mathrm{mm\,h^{-1}}$ im Neckartal höher, was auf ein häufigeres Auftreten von Starkregenereignissen dort hindeutet.
Eine Zeitreihe der Regenrate, die von den Parsivels in-situ aufgezeichnet wurde, wird mit den Beobachtungen eines X-Band-Radars für die der Superzelle vom 23. Juni 2021, verglichen. Wie erwartet, bestätigt sich die zeitliche Übereinstimmung zwischen der in-situ-Messung und der Beobachtung des Radars. Außerdem zeigen die Zeitreihen von der Regenrate und dem typischen Tropfendurchmesser für den Durchgang der Superzelle über Rottenburg eine starke zeitliche Variabilität innerhalb des Ereignisses.

Contents

1 Introduction and motivation

The drop size distribution (DSD) is an essential property of precipitation and among the easily observable consequences of rain microphysics. There are multiple meteorological applications for DSDs, e.g. in radar meteorology or in the description of microphysical processes of precipitation systems such as winter storms or tropical storms (Tokay et al., 1999; Schuur et al., 2001; Yuter et al., 2006; Tokay et al., 2008). Other applications include the evaluation of the impact of DSDs on soil erosion or even the effect the distribution has on rainwater penetrating buildings during extreme wind events (Azevedo Coutinho and Pereira Tomás, 1995; Lopez et al., 2011).

Dual polarization radars can provide indirect information on DSD and hydrometeor type of precipitation. However, remote sensing measures large volumes and therefore radars depend on integral quantities as e.g. reflectivity, frequency Doppler shift (providing information on the speed of probed particles) and polarimetric information of the scattered electromagnetic waves (Ryzhkov, 2019). Interpretation of active remote measurements like radar measurements always poses an inverse problem. To infer the atmospheric state from the measurement, one cannot avoid making simplifying assumptions that are not always well met. Furthermore, rain rate is not among the measured properties. It has to be deduced from the radar measurements, e.g. by the non-physical Z/R-relation. All this makes radar observations susceptible to errors. Ground truth measurements of DSDs provide a reference to validate radar-based estimates (Goddard et al., 1982; Schuur et al., 2001; Adirosi et al., 2020; Conrick et al., 2020). Additionally, they are a means to improve the accuracy of radar retrievals such as the quantitative precipitation estimation (QPE), which is a method to approximate precipitation intensity (Brandes et al., 2004). However, ground truth measurements with rain gauges are also fraught with difficulties. These include too much or too little rain as well as strong winds that distort the record of precipitation totals. Further problems arise from equipment maintenance and the lack of representativeness of the measurements.

The widely used Parsivel (Particle Size and Velocity) disdrometer (Löffler-Mang and Joss, 2000; Friedrich et al., 2013b; Thompson et al., 2015; Chen et al., 2017; Ji et al., 2019; Chen et al., 2020; Liu et al., 2021) provides such in-situ DSDs and other precipitation properties by determining the size and fall velocity of particles falling through its measuring area.

In this Master's thesis data collected in the framework of the Swabian MOSES (Modular Observation Solutions for Earth Systems) (KIT, 2021) field campaign was used to measure and investigate DSDs. The Swabian Jura and the Neckar Valley in the south-west

of Germany is an area susceptible to hydrometeorological extremes. It displays the most frequent thunderstorms with hailfall activity in Germany (Fluck et al., 2021). Heat waves and droughts are also common phenomena in this region. To better understand how such phenomena arise and to improve their prediction, the field campaign Swabian MOSES has been conducted there during summer 2021. The campaign is a combined effort by a large number of institutions, with the Institute of Meteorology and Climate Research (IMK) of the Karlsruhe Institute of Technology being the lead contributor. Countless measuring systems were used to investigate the atmospheric conditions, including a network of 23 Parsivel disdrometers at 18 different sites. This network is an integral part of KITcube, a mobile integrated atmospheric observation system operated by the Department of Troposphere Research of the IMK. The instrumentation of the KITcube also incorporates a dual-polarisation X-band radar, which enables the above mentioned comparisons between radar estimates and in-situ measurements in future studies.

Apart from Liu et al. (2021), who had 34 Parsivels, but distributed over a much larger area compared to the Swabian MOSES campaign, no experiment is known with such a large number of Parsivels in operation. The dense network enables an examination of the spatial variability of DSDs with a one of a kind high resolution.

The Parsivel network was used for the first time in this experiment. Therefore, a quality control had to be developed first (subsection 3.4.1). The interest of this thesis is in summer precipitation events with heavy impacts on common welfare. However, the measurements show in the vast majority of events moderate, weak or even very weak precipitation. The characteristics of these weak precipitation events can only be determined with large errors because few hydrometeors are recorded here. Excluding the many weak events from the analysis is therefore a first step to be able to focus on relevant measurements (section 4.1).

The measurements at sufficient precipitation intensity are then evaluated to describe the drop spectrum with a few parameters. Here the normalized gamma distribution (Testud et al., 2001; Illingworth and Blackman, 2002) is utilised as a mathematical model. The accuracy with which these parameters can be determined is investigated by comparing measurements from neighbouring Parsivel instruments. The minimum requirement that the differences of synchronous, collocated measurements must remain small compared to the natural variability of these parameters during the whole experiment must be met (subsection 3.4.3).

Based on these preliminary investigations, the properties of the precipitation can then be analyzed. In particular, the mutual dependence of the determined parameters on each other can be examined (section 4.1). First, it is a matter of investigating these dependencies for the entire experiment. By defining three parameters, the description of the gamma distribution is complete. In principle, one would like these three parameters to be independent of each other, i.e. to represent independent properties of the drop spectrum. For practical application, it is particularly relevant how the parameters behave relative to the rain rate.

The spatial distribution of the Parsivels during this experiment allows an analysis of the spatial variability of the determined parameters (section 4.2). Is there an effect of the orography of the measuring area on the properties of precipitation? In what properties of precipitation can an effect of orography be found?

Finally, the data measured during the occurrence of a supercell with heavy rain and hailfall on June 23, 2021 causing massive damage in the measuring area is analysed. Based on this incident of unusual intensity, the temporal agreement of ground truth measurements by the Parsivels and remote sensing by the X-band radar is tested (section 4.3).

To summarize, the specific objectives of this thesis are the following: One is the control of the quality of the Parsivel network, which was used for the first time. Determining the DSD from disdrometer measurement is in principle prone to statistical errors due to small sample sizes (Kann et al., 2015; Jaffrain and Berne, 2011). Additional imperfections because of instrument limitations easily lead to unusable measurements. Based on a comparison of simultaneously measured DSD of collocated Parsivels, these uncertainties can be quantified.
Another goal is the investigation of the interdependencies of the parameters of the gamma distribution. The gamma distribution has three parameters. The intent is to find a description where these three parameters are statistically independent in observed rain. In that case the three parameters describe three different properties that might have a physical meaning. The dependencies have been investigated in previous studies (e.g. (Chen et al., 2016; Liu et al., 2021)). With this thesis the rain properties from an additional region can be added.
Orography has an impact on the development of precipitation. This leads, among others, to known local variations in the spatial distribution of rain and thunderstorms. Investigating how these variations are represented in the DSD is yet another goal. Knowledge on the impact of orography on DSD could help to improve radar products, such as QPE.

This thesis is divided into five sections. Following the introduction, the theoretical concepts of the formation of DSDs at ground-level and the gamma distribution are explained. Subsequently, the data acquisition, which includes the experimental setup, the introduction of the measuring device as well as the data processing, is addressed in the third chapter. In chapter four, the results of this thesis are presented. A summary and conclusions of this work are given in the final chapter.

2 Theoretical concepts

2.1 Drop size distribution

The drop size distribution (DSD) is a fundamental property of precipitation. It states the number of drops $n(D)\,\mathrm{d}D$ in a diameter range between D and $D + \mathrm{d}D$ per unit volume. This distribution $n(D)$ is of great interest because it is needed to determine, for example, the rain rate R or the reflectivity factor Z of rain:

$$R = \frac{\pi}{6} \int_0^\infty v(D) n(D) D^3 \,\mathrm{d}D\,, \tag{2.1}$$

and

$$Z = \int_0^\infty n(D) D^6 \,\mathrm{d}D\,, \tag{2.2}$$

with the terminal fall velocity of drops $v(D)$ (Rogers and Yau, 1996). Radars can only measure Z, which depends on the 6th power of D. The non-physical approximation $Z = aR^b$ is used to estimate the rain rate, with Z given in $\mathrm{mm^6\,m^3}$ and R in $\mathrm{mm\,h^{-1}}$. This relationship is known as the Z/R-relationship. a and b are empirically determined factors and vary with atmospheric conditions as well as type of precipitation. Due to the dependency of Z and R on $n(D)$, radar meteorology profits from a precise knowledge of the shape of the DSD (spectral shape) of rain.

The following section explains the critical processes that contribute to the shape of DSDs at ground level. Precipitation formation directly influences the spectral shape of rain, including processes that take part in the development of clouds and the growth of ice particles and raindrops therein. However, the majority is masked by processes taking place while the drops fall to the ground.
The change in the DSD shape below the cloud base is affected by processes that mainly depend on meteorological variables such as temperature, relative humidity and wind. A particularly strong contribution to changes in the DSD brings the alteration of the number density of small drops. The number of small drops increases through larger drops breaking up during sedimentation. This effect gets partially compensated by the collection of small drops through larger drops, coalescence of drops, or complete evaporation of small drops (Pruppacher and Klett, 1997).
The area in which the DSD is influenced most notably below the cloud is referred to as the bright band in radar meteorology. Falling ice particles start melting when the temperature

of the surrounding air is warmer than 0°C. However, the melting takes place over several hundred meters because of the limited rate the latent heat of the ice phase particles can dissipate in the surrounding air. Therefore, the hydrometeors are typically melted completely at about 5°C. In the melting process, the ice particles are covered by a thin layer of water. This leads to a hydrometeor with the size of an ice particle and the reflectivity of water Pruppacher and Klett (1997).
Due to its larger dielectric constant, water is a better backscatterer than ice, as can be seen, e.g., from the scattering amplitudes in the Rayleigh approximation (Ryzhkov, 2019). The water-covered ice particle results in an increased scattering of the electromagnetic waves of the radar and subsequently in a jump in reflectivity (Pruppacher and Klett, 1997). The term bright band comes from the single-color analogue displays which were used in the early days of radar technology that represented reflectivity through brightness. Thus, the area with increased reflectivity was seen as a bright band on the screen.
Shortly before the melting starts, snow crystals typically aggregate to big sizes of up to 5 to 10 mm. The fall speeds of these large particles are about 1 to 2 $\mathrm{m\,s^{-1}}$. Other ice particles such as hailstones or graupel, which also result in the bright band when they melt, fall at higher velocities. During the passing of the bright band, ice particles can break up under certain conditions. When melting the ice particles turn into drops, typically with diameters between 1 and 2.5 mm. In comparison to snowflakes, the melted drops have very different aerodynamics resulting in larger fall velocities. The drops of typical diameters have fall velocities between 4 to 8 $\mathrm{m\,s^{-1}}$ (Pruppacher and Klett, 1997).
Assumptions about cloud physics based on DSDs measured at ground level are in general afflicted with high uncertainty due to the multitude of the above-mentioned processes taking place. However, it is possible to gain cloud information from ground-level DSDs. For example, Thompson et al. (2015) as well as Ji et al. (2019) have been working on a parameterization of DSDs in order to deduce a reliable method to differentiate between convective and stratiform precipitation.

In general, raindrops are found in a size range of up to 5 mm in diameter. In some rare instances, drops of up to 8 mm have been reported (Beard et al., 1986; Chen et al., 2020). But even in laboratory conditions, drops never exceed about 10 mm because they become hydrodynamically unstable. Generally, drop sizes of more than 2 to 3 mm are rare if not for thunderstorms or rain events with rain rates larger than 50 $\mathrm{mm\,h^{-1}}$.
Raindrops smaller than 0.28 mm are almost perfect spheres because the surface tension forces are predominant (Pruppacher and Beard, 1970). Drops with a diameter between 0.28 and 1 mm start taking the form of oblate ellipsoids due to hydrostatic pressure gradient within the drop and aerodynamic forces coming into effect (Pruppacher and Klett, 1997). Yet, the effects in that size range are so small that drops can still be well approximated as spheres. For drops with $D > 1$ mm the aerodynamic forces play larger role. The deforming results in a shape of an oblate ellipsoid with a flat base. Figure 2.1 shows the shape of drops with different diameters. Drop diameters are mostly given in volume-equivalent diameters to account for this change in shape.
Drops of ellipsoidal shape oscillate between an oblate and a prolate form, but spend the

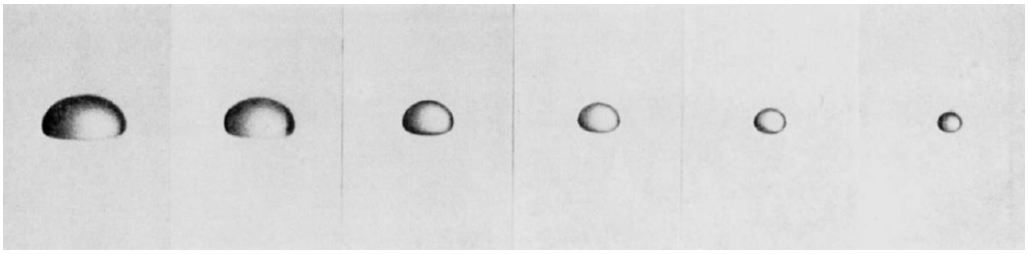

Figure 2.1: Shapes of raindrops of different volume-equivalent diameter falling at their terminal velocity. The diameter in mm from right to left is: 1.35, 1.725, 2.65, 2.90, 3.675 and 4.00. This graphic is taken from Pruppacher and Beard (1970).

larger amount of time in the oblate form because of its higher stability (Pruppacher and Klett, 1997).

Their different sizes and therefore different weights and shapes result in different terminal fall velocities. The fall velocity is determined by the interplay of the gravitational force and the upward acting frictional force. In-situ conditions make it impossible to analytically approach the relationship of terminal fall speed v_t and diameter D. There are many different attempts to determine $v_t(D)$. In this work the commonly used empirical relation found by Atlas et al. (1973) will be used:

$$v_t(D) = v_{\max} - v_1 \exp(-\alpha D)\,, \tag{2.3}$$

with $v_{\max} = 9.65\,\mathrm{ms}^{-1}$, $v_1 = 10.3\,\mathrm{ms}^{-1}$ and $\alpha = 0.6\,\mathrm{mm}^{-1}$.

A drop size and velocity distribution (DSVD) is needed to calculate DSD parameters (section 3.3) from the data recorded by the measuring device used in this thesis because it classifies drops on the basis of both these parameters. This distribution states the number of drops $n(D, v)\,\mathrm{d}D\,\mathrm{d}v$ in a diameter range between D and $D + \mathrm{d}D$ and a velocity range between v and $v + \mathrm{d}v$ per unit volume.

2.2 Analytical description of the DSD

Different approaches have been made to describe the DSDs analytically, e.g. by Marshall and Palmer (1948); Feingold and Levin (1986); Torres et al. (1994). Historically, the most commonly used frequency distribution was the one established by Marshall and Palmer (1948):

$$n(D) = N_0 \mathrm{e}^{-\lambda D}\,, \tag{2.4}$$

with the intercept parameter N_0 and the slope parameter λ. They believed that the intercept parameter is a constant and could be determined by an extrapolation of this exponential distribution to $D = 0\,\mathrm{mm}$. This resulted in the empirically found value $N_0 = 8 \times 10^3\,\mathrm{m}^{-3}\mathrm{mm}^{-1}$. They also found that the slope parameter is directly related to the rain rate in the following manner: $\lambda = 4.1 R^{-0.21}\mathrm{mm}^{-1}$. The constant N_0 and the assumption

that λ only depends on R enabled them to deduce values for the factor a and the exponent b of the above-mentioned Z/R-relationship $Z = aR^b$.
In later works on the description of DSDs it was shown that N_0 is not a constant and that λ can take other values (e.g. Sekhon and Srivastava (1971)). DSDs of samples measured over long intervals, say one hour, are still well described by the Marshall-Palmer distribution, if the parameters N_0 and λ are adapted.
However, for samples measured over short intervals, say one minute or less, it was shown that the maximum of DSDs was at a value $D > 0\,\text{mm}$ (e.g. Willis (1984)). To account for this observation, the gamma distribution, a frequency distribution with three parameters, was introduced to describe the drop spectrum:

$$n(D) = N_0 D^{\mu} \mathrm{e}^{-\lambda D}\,. \tag{2.5}$$

The additional shape parameter μ enables to describe a decrease in number concentration of small drops. Evaluating DSDs of one-minute samples is common practice nowadays. The gamma distribution is the most widely used analytical description of the size spectra of raindrops in recent works on this topic (Willis, 1984; Testud et al., 2001; Illingworth and Blackman, 2002; Smith and Kliche, 2005; Kliche et al., 2008; Cao and Zhang, 2009; Mallet and Barthes, 2009; Liu et al., 2021).

Limiting sample intervals to one minute does not come without problems. Short intervals lead to DSDs where the number of the rarer large drops ($D > 3\,\text{mm}$) is so small that statistical errors become significant (Handwerker and Straub, 2011; Jaffrain and Berne, 2011), which is especially problematic since reflectivity is a function of 6th power of the drop diameter (Equation 2.2). Therefore, large drops contribute significantly more to the reflectivity factor Z than small drops do. Thus, the reflectivity factor Z deduced from such DSDs is potentially flawed. This circumstance is known as "sampling problem".

An unphyiscal property of the gamma distribution is the dimension of N_0: length$^{-4-\mu}$. It depends on μ and this should not be the case if the parameter carries a physical meaning. The intercept parameter N_0 also strongly correlates with μ, which further indicates the suboptimal choice of the three parameters N_0, μ and λ.
Instead the more intuitive parameters N_L, D_0 and μ can be used preferably. The normalized intercept parameter N_L will be introduced by the end of this section. A typical drop diameter, such as D_0, can be defined in different ways. One possibility is the median volume diameter, that splits the liquid water content (LWC) in two. That means all drops smaller than the median volume diameter D_0 of one measured sample contain as much water as all drops larger than D_0:

$$\frac{\pi}{6}\int_0^{D_0} n(D) D^3\,\mathrm{d}D = \frac{\pi}{6}\int_{D_0}^{\infty} n(D) D^3\,\mathrm{d}D\,. \tag{2.6}$$

To calculate the median volume diameter the numerically found relationship suggested by Ulbrich (1983) is adopted:

$$D_0 = \frac{\mu + 3.67}{\lambda}\,. \tag{2.7}$$

D_0 is solely dependent on parameters of the gamma distribution and thus, a property thereof.

A frequency distribution, such as $n(D)$, can be described by its moments, which are defined as:

$$M_i = \int_0^\infty n(D) D^i \,\mathrm{d}D\,. \tag{2.8}$$

For the gamma distribution this becomes:

$$M_i = N_0 \frac{\Gamma(\mu + i + 1)}{\lambda^{\mu+i+1}}\,, \tag{2.9}$$

with the Gamma function Γ (e.g. Vivekanandan et al. (2004)). Important physical properties of precipitation can be expressed as moments of this distribution. M_0 is the total amount of drops per unit volume N_t. M_3 multiplied by the constant factor $\frac{\pi}{6}\rho_\mathrm{w}$, with ρ_w as the density of water, is the liquid water content (LWC). M_6 is the radar reflectivity factor Z (Equation 2.2). Although the rain rate R is not represented by one of the moments, the fourth moment, M_4 is often taken as an approximation of R.
These moments can vice versa be used to determine the parameters of a DSD. As there are three parameters, three moments are sufficient. The equivalence of moments and precipitation characteristics enables the determination of the moments from the measured quantities. The choice of the three moments M_k, M_l and M_m ($0 \leq k < l < m$) that are used to determine the three parameters N_0, μ and λ of the gamma distribution is arbitrary:

$$\frac{[(\mu + m)...(\mu + l + 1)]^{l-k}}{[(\mu + l)...(\mu + k + 1)]^{m-l}} = M_m^{l-k} M_l^{k-m} M_k^{m-l}\,, \tag{2.10}$$

$$\lambda = \left[\frac{M_k}{M_m}\frac{\Gamma(\mu + m + 1)}{\Gamma(\mu + k + 1)}\right]^{\frac{1}{m-k}}\,, \tag{2.11}$$

$$N_0 = M_l \frac{\lambda^{\mu+l+1}}{\Gamma(\mu + l + 1)}\,. \tag{2.12}$$

Intuitively, it seems obvious to use the moments M_0, M_3 and M_6, representing precipitation properties, to calculate the parameters. But moments correlate strongly and therefore parameters vary depending on the chosen combination of moments used. The accuracy of various different moment combinations has been examined by, for example Smith and Kliche (2005) and Handwerker and Straub (2011). In this work the three lowest moments $i = 0, 1, 2$ will be used, following the recommendation of Handwerker and Straub (2011). The good performance of the lowest three moments is a consequence of the sampling problem mentioned above. Higher moments are stronger biased by the sampling problem

because of the proportionality $M_i \propto D^i$.
Taking the first three moments with $k = 0$, $l = 1$ and $m = 2$, the equations 2.10, 2.11 and 2.12 represent an analytically solvable system of equations which yields the following expressions for the parameters μ, λ and N_0:

$$\mu = \frac{1}{\frac{M_0 M_2}{M_1^2} - 1} - 1\,, \qquad \lambda = \left[\frac{M_0}{M_2}(\mu+2)\right]^{\frac{1}{2}}\,, \qquad N_0 = M_1 \frac{\lambda^{\mu+2}}{\Gamma(\mu+2)}\,, \tag{2.13}$$

for $M_1^2 \neq M_0 M_2$ and $M_2 \neq 0$.

This approach to determine the parameters of the gamma distribution is called the "moments method" (Handwerker and Straub, 2011). There are also other methods; e.g. the maximum likelihood method as suggested by Haddad et al. (1997). However, for the samples at hand, the moments method is best suited, even though this method is inherently biased (Smith and Kliche, 2005).

The gamma distribution $n(D)$ has the dimension length^{-4}. Its parameters have the following dimensions: λ has length^{-1}, μ has dimension one and N_0 has length$^{-4-\mu}$. To avoid the above mentioned problematic dependency of N_0 on μ, the gamma distribution can be normalised. The moments mentioned above are used for this purpose. Rearranging Equation 2.9 for N_0 yields:

$$N_0 = M_i \frac{\lambda^{\mu+i+1}}{\Gamma(\mu+i+1)}\,. \tag{2.14}$$

Inserting this expression for N_0 in the gamma distribution, one obtains:

$$n(D) = M_i \frac{\lambda^{\mu+i+1}}{\Gamma(\mu+i+1)} D^\mu \mathrm{e}^{-\lambda D}\,. \tag{2.15}$$

The problem with this equation is that M_i does not have the desired dimension length^{-4}. To establish the normalized gamma distribution as an expansion of the historically common Marshall-Palmer distribution, Equation 2.15 should yield the Marshall-Palmer distribution for $\mu = 0$, so that $N_i = N_0$. To achieve this the following factor is introduced, anticipating the next step of normalization (Illingworth and Blackman, 1999):

$$M_i = N_i \frac{i!}{3.67^{i+1}} D_0^{i+1}\,. \tag{2.16}$$

In order to get the desired dimension and to reduce the correlation with μ, Illingworth and Blackman (1999) suggested a normalization with the liquid water content (M_3) so that:

$$n(D) = \underbrace{\frac{3!}{3.67^4}}_{=0.033} N_L \frac{\lambda^{\mu+4} D_0^4 D^\mu}{\Gamma(\mu+4)} \mathrm{e}^{-\lambda D}\,, \tag{2.17}$$

with the normalization factor of the third moment $N_L = \frac{3.67^4 M_3}{6 D_0^4}$ obtained by transposing Equation 2.16. N_L has the desired dimension of length^{-4} and the interdependency of the three parameters N_L, λ and μ is now weak.

3 Data acquisition and methods

3.1 Experimental setup

3.1.1 Swabian MOSES field campaign

The Swabian Jura and the Neckar Valley in the south-west of Germany are the areas with the most frequent hail events in this country (Puskeiler et al., 2016; Schmidberger, 2018). The area is densely populated and the Neckar Valley is heavily industrialised, which leads to high financial risks, but more importantly, risks of population health. In addition to these factors, the region shows some interesting orographic features, too. It has a large altitudinal gradient, up to 1016 m MSL on the Jura and down to about 290 m MSL in the Neckar Valley at Nürtingen, and a versatile soil type profile, to name just two.

For the above-mentioned reasons, this area is extremely interesting for a research campaign on heavy precipitation. A large body of institutions realised such a field campaign with Swabian MOSES. The institutions invlolved are: Institute of Meteorology and Climate Research (IMK) of the Karlsruhe Institute of Technology (KIT), Helmholtz Center for Environmental Research (UFZ), Technical University of Braunschweig, Research Center Jülich (FZJ), Eberhard Karls University of Tübingen with the CRC 1253 CAMPOS, University of Hohenheim, Helmholtz Center Potsdam - German Research Center for Geosciences (GFZ), German Weather Service (DWD), German Aerospace Center (DLR) and Center of Solar Energy and Hydrogen Research Baden-Württemberg (ZSW).

The campaign aimed to observe two different hydro-meteorological extremes. First, the occurrence of convective storms, ideally with heavy rainfall and hail, as indicated earlier. Secondly, the appearance of large-scale heat waves and droughts. Both these events typically occur in summer, which is why the campaign was conducted from May to September 2021. The intense measuring phase, where the focus was on convection cells, thunderstorms and related weather phenomena was from Mai to July 2021. During this period a mobile team was on alert at all times to start an IOP (intensive operation phase). An IOP meant regular radiosoundings every three hours (or more frequent) and an advanced ability to deal with problems of the observation system immediately when they occurred.

The observation system MOSES is a new highly flexible observation system of the Helmholtz Association consisting of mobile sub-systems (e.g. KITcube) (Weber et al., 2022). The range of measuring devices used in the Swabian MOSES campaign is huge.

X-Band radar, cloud radar, cloud camera system, microwave-radiometer, energy balance station, radiosondes, swarm sondes, Lidar-network, meteorological stations, Parsivel network and hail sensors are just the devices that belong to the mobile KITcube module, which was based near Rottenburg, located southwest of Tübingen (Figure 3.1). Additional data came from aerosol measuring systems, balloon soundings, stream surveys, an infrasound sensor and the MoLEAF (Mobile Land-Ecosystem-Atmosphere Flux) Tower. On days of interesting convection, when thunderstorm activity was not too strong, two research aircraft did also collect full meteorological data, such as temperature and moisture at high temporal resolution for turbulence investigations. This multitude of instruments allows for a very complete assessment of atmospheric parameters and helps to analyse the whole chain of events related to a certain weather phenomenon. What triggers the event? How does it develop? What are its effects? How does it subside? And why sometimes nothing happens, despite the prediction of convection? These are some of the questions this campaign aimed to answer.

3.1.2 Parsivel network

Embedded in the KITcube observation system is a disdrometer network of 23 Parsivels, which acquired the data used in this thesis. From this measured data DSDs and other precipitation properties are deduced. A detailed discription of the instrument and its measuring method is given in the next section (section 3.2). The 23 Parsivels were setup at 18 different locations (Figure 3.1). 15 measuring sites are distributed between 8.83° to 9.43° E and 48.33° to 48.63° N, densely covering a highly populated part of the Neckar Valley and the Swabian Jura including the transition of the two areas. The northern edge of the measurement area is observed by the device located in Friolzheim at 48.83° N. Convective cells often form over the Black Forrest (Weckwerth et al., 2011) and can then move northeast through the Neckar Valley. That's why the measuring site at Bettenhausen, close to the eastern slopes of the Black Forrest, but still near the Neckar, marking the westermost measuring point at 8.55° E, is important. One Parsivel was set up far to the south of the other sites near Donaueschingen at 47.95° N. Due to technical issues, this Parsivel needed replacement, leading to a much smaller body of data for this site, which is why this Parsivel is not considered in this thesis.
Three locations were equipped with two Parsivels and one with three, allowing an intercomparison of the devices without accounting for the varying conditions at different sites. The large number of densely distributed modern disdrometers over large parts of the measuring region ensures very good coverage of any precipitation-related phenomena during this campaign. An altitude range from 286 m MSL to 780 m MSL was covered by the Parsivel sites. All Parsivels with their exact location are listed in Table 3.1. The data set was recorded from April 15, 2021 to October 8, 2021.

Table 3.1: Exact locations and elevations of all Parsivels sorted by elevation. In brackets are the short names of the devices. These make later plots clearer.

Parsivel Name	Latitude in °	Longitude in °	Elevation in m MSL	Location
PARS2020L (Pl)	48.5958	9.2431	286	Neckartenzlingen
PARS2020O (Po)	48.5681	9.2272	292	Mittelstadt
PARS2020S (Ps)	48.5940	9.2974	309	Großbettlingen
PARS2017A (Pu)	48.4892	8.9550	336	Rottenburg
PARS2019A (Pv)				
PARS2020A (Pa)				
PARS2020M (Pm)	48.5022	9.1659	337	Betzingen
PARS2020R (Pr)	48.4819	9.0650	346	Dußlingen
PARS2019B (Pw)	48.6279	9.2993	368	Nürtingen
PARS2020B (Pb)				
PARS2020N (Pn)	48.4738	9.1905	401	Ringelbach
PARS2020D (Pd)	48.5132	9.3676	419	Dettingen
PARS2020I (Pi)	48.8314	8.8291	448	Friolzheim
PARS2020C (Pc)	48.3760	8.5534	457	Bettenhausen
PARS2020H (Ph)	48.5768	9.4278	457	Owen
PARS2020G (Pg)	48.3891	8.8351	484	Haigerloch
PARS2020T (Pt)				
PARS2020Q (Pq)	48.3393	9.3215	737	Hohenstein
PARS2020K (Pk)	48.4400	9.3169	764	Ohnastetten
PARS2020E (Pe)	48.3353	9.1061	772	Burladingen
PARS2020F (Pf)				
PARS2020P (Pp)	48.3889	9.1769	780	Sonnenbühl

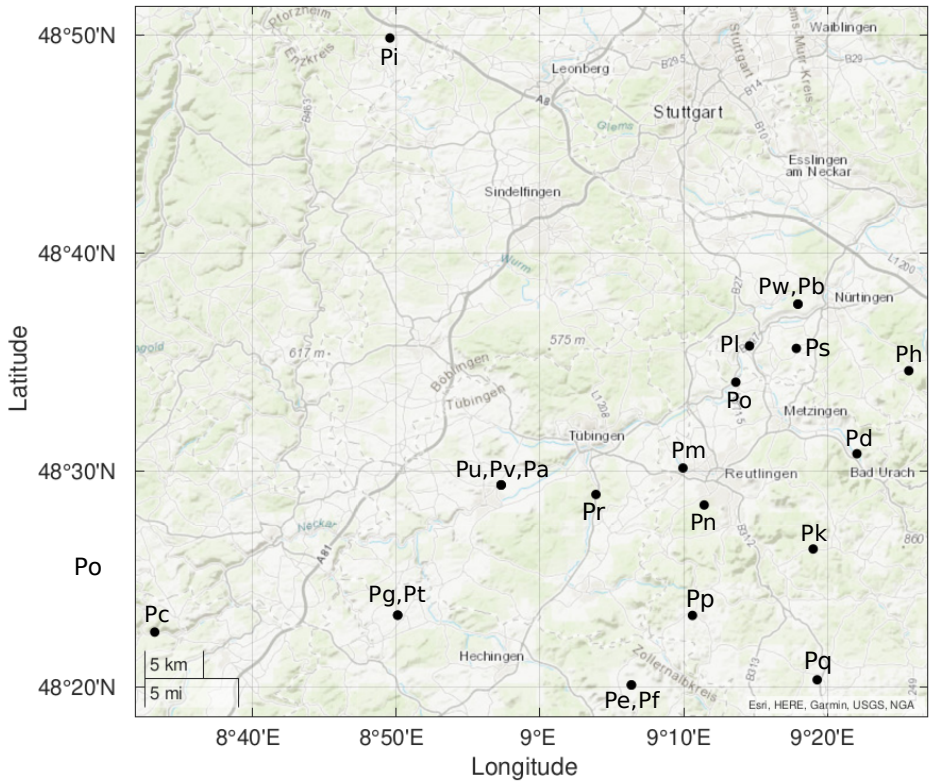

Figure 3.1: The locations (dots) of the measuring sites with the respective Parsivels present.

3.2 Laser optical disdrometer

3.2.1 Measuring method

A laser optical disdrometer measures size and fall speed of hydrometeors. It creates a light band with a well-defined area and thickness between a laser and a receiver. When a hydrometeor passes through the light band, it blocks a fraction of it due to absorption and scattering. The partially blocked light beam leads to a reduced voltage output of the receiver. The reduced voltage output relates linearly to the shadowed fraction of the light sheet (Löffler-Mang and Joss, 2000).

Due to the thickness of the light beam, the attenuation of the signal is not instantly, but rather takes a specific shape for each individual hydrometeor depending on its size, fall velocity and shape. Two examples can be seen in Figure 3.2. These examples highlight the difference between small and large drops. The cross-section area of small drops, with a diameter smaller than the light band thickness (one millimeter), is proportional to the maximum blocked area of the drop transit. For drops with a diameter larger than one millimeter, it is the horizontal expansion that is proportional to the blocked area.

As illustrated in part (b) and (c) of Figure 3.2, the amplitude of the signal deviation provides the size of the particle (Löffler-Mang and Joss, 2000).

The signal duration provides the fall speed of the hydrometeor. The particle affects the

light beam and therefore the signal from the moment it enters the beam until the moment it has entirely left the beam. The distance the particle covers while affecting the light beam is the light band thickness plus the particle diameter (see Figure 3.2). The fall velocity is determined by the quotient of this distance and the signal duration.
As described in section 2.1, liquid drops larger than one millimeter in volume-equivalent diameter are not spherical in shape but oblate ellipsoids. If the measured horizontal diameter, which in the case of an oblate ellipsoid is larger than the vertical one, was used for the calculation, the fall velocity would be overestimated. Thus, the drop geometry is taken into account in order to obtain the correct speed (Löffler-Mang and Blahak, 2001).
Drops smaller than one millimeter are calculated as spheres. Drops between volume-equivalent diameters of 1 mm and 5 mm are considered to decrease linearly from 1 to 0.7 in axial ratio (height over width). The axial ratio of particles with diameters larger than 5 mm is taken as constant at 0.7 (Battaglia et al., 2010).
Information of the fall speed and size of the hydrometeors enable the Parsivel to identify the precipitation type by comparing it with the relation of fall speed and size v(D) of liquid drops. This is schematically shown in Figure 3.3 from Löffler-Mang and Joss (2000). Hailstones, for example, can reach larger sizes and therefore higher fall velocities than raindrops, which is why hail is found above the liquid drop curve at hydrometeor sizes bigger than 5 mm in the schematic. Snow on the other hand, covering almost the entire size range, sediments slowly due to its high air resistance and is therefore distinguishable from liquid drops. For larger drops this distinction becomes especially clear because of the large difference in fall velocity between snowflakes and raindrops.

3.2.2 Parsivel

The data used in this work is measured by the laser optical Parsivel disdrometer (Figure 3.4), originally developed by Martin Löffler-Mang and now produced by OTT HydroMet. A laser diode (wavelength: 650 nm, output power (peak): 0.2 mW) creates a light band between itself and an optical sensor, each located in a separate housing attached to a V-shaped metal mount. On each housing there is a thin perforated metal sheet to disperse raindrops in order to prevent secondary hydrometeors from rebounded drops to fall through the measuring surface. The light beam is 30 mm wide and 1 mm thick. The distance of the two sensor heads is 180 mm resulting in a measuring surface of 180 mm $\times$ 30 mm $\left(54\,\mathrm{cm}^2\right)$.

Each measured particle is classified into 32 non-equidistant size classes and 32 non-equidistant velocity classes. To make particles of varying forms comparable, the size is specified as volume-equivalent diameter. A low signal-to-noise ratio is the reason why the smallest two size classes are not used at all. Although always empty, they are considered in the calculations. The smallest measurable particle diameter is 0.25 mm and 25 mm is the maximum. The maximum measurable size of liquid drops is 8 mm, while the size range used for solid particles includes the maximum. The size class width is ranging from 0.125 mm to 3 mm. The velocity classes range from 0.05 (mid-value of class) to

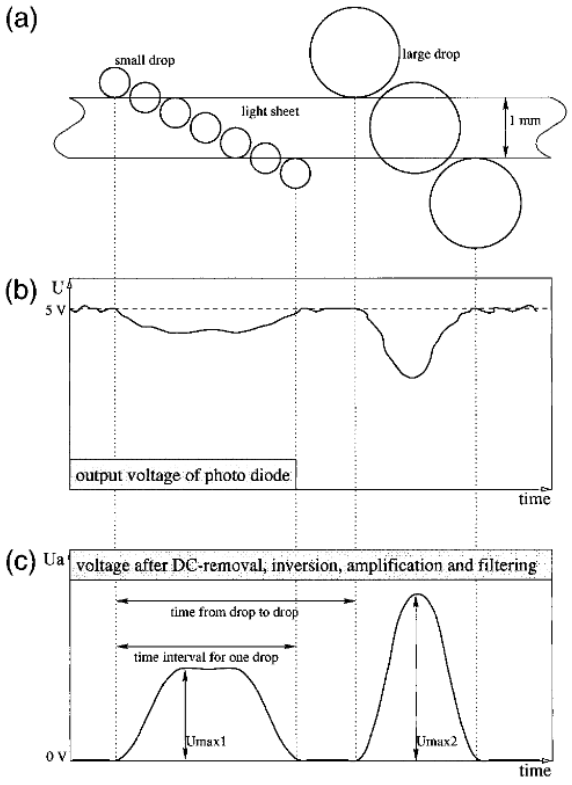

Figure 3.2: Measuring process taken from Löffler-Mang and Joss (2000). (a) A small and a large hydrometeor passing through the light band. (b) Unprocessed voltage output of the sensor. (c) Inverted, amplified and filtered signal.

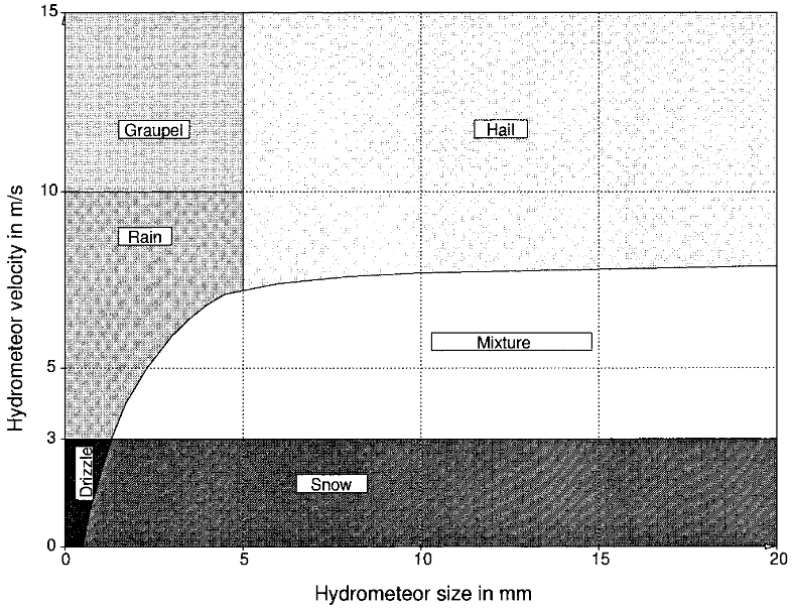

Figure 3.3: Identification schema to determine the precipitation type using size and fall speed taken from Löffler-Mang and Joss (2000). The hydrometeors get classified by comparison to a reference terminal fall velocity $v(D)$.

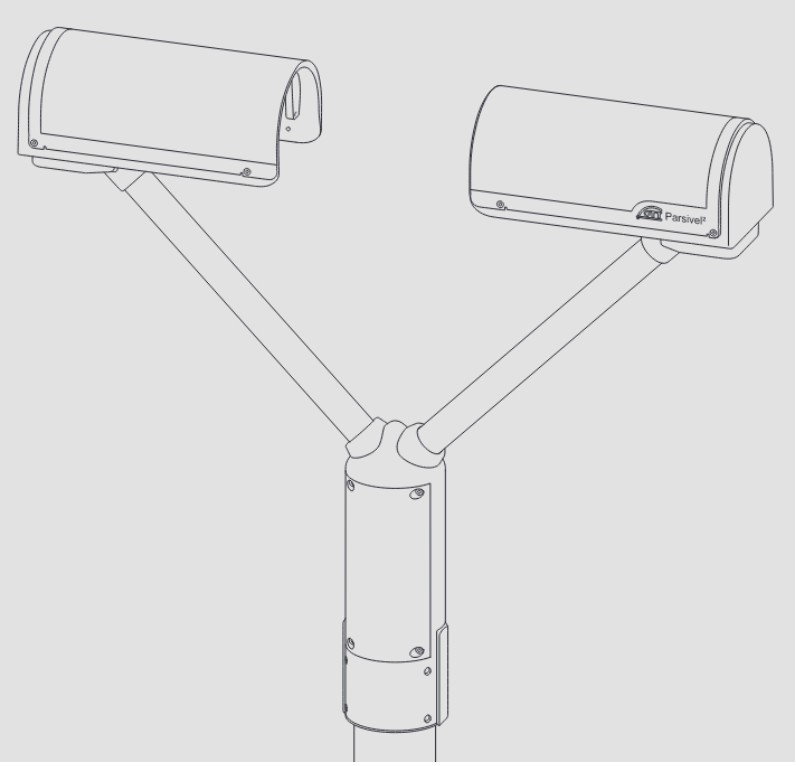

Figure 3.4: Technical drawing of the Parsivel (OTT-HydroMet, 2022).

20.8 m s^{-1}, with a maximum detectable speed of 22.4 m s^{-1} due to a class spread ranging from 0.1 to 3.2 m s^{-1} . The drops are assigned the value of the center of the class they are in. All size and velocity classes can be found in Table A.7 and Table A.8 taken from the manual (OTT-HydroMet, 2022).

The classified particles are output in a 32×32 matrix, providing 1024 different categories. Multiple quantities can be retrieved from this data by the Parsivel itself, e.g. rain rate R, reflectivity Z and the total number of drops N. In this thesis Z and N are used for quality control of the data (subsection 3.4.1). The rain rate is calculated with own retrievals (section 3.3) because it has been shown that the rain rate can be calculated more accurately if determined with quality-controlled data (Liu et al., 2021).

3.3 Data processing: calculation of moments and other parameters

The number of particles in a size interval $[D_i,\ D_i + \Delta D_i]$ and a fall velocity interval $[v_j,\ v_j + \Delta v_j]$ is given by $n(D_i, v_j)\Delta D_i \Delta v_j$, with the DSVD $n(D_i, v_j)$. Within a time interval Δt the sedimenting drops cover a distance of $\Delta t\, v_j$. The number of particles c_{ij} with the size D_i and the velocity v_j falling through the measuring surface A_i during the time interval Δt is given by:

$$c_{ij} = n(D_i, v_j)\Delta D_i \Delta v_j\, A_i\, \Delta t\, v_j\,. \tag{3.1}$$

For the drop number density, however, the fall velocity is of no relevance, which is why the 32 velocity classes are summed up:

$$n(D_i) = \sum_{j=1}^{32} n(D_i, v_j)\,\Delta v_j = \sum_{j=1}^{32} \frac{c_{ij}}{A_i \Delta t\, v_j\, \Delta D_i}\,. \tag{3.2}$$

As with most high-resolution precipitation observations, the sampling time Δt was set to one minute. Intervals of less than a minute are problematic because of the before mentioned sampling problem and DSDs with μ shifted to larger values, poorly representing the underlying drop population. The Parsivel was set to measure with a resolution of 15 seconds. A moving integration enables the required one minute spectra.

The dependency of the measuring surface A (subsection 3.2.2) on the ith size class arises from its susceptibility to border-effects, which are drops that fall through the light band only partially and therefore get classified falsely. To mitigate this effect, Jaffrain and Berne (2011) suggest the following correction, which is used in this thesis: $A_i = 180\,\text{mm} \times (30\,\text{mm} - 0.5 D_i)$.

For further evaluation the following characteristic DSD parameters are determined: total amount of drops N_t (= M_0), rain rate R and the moments M_1, M_2 and M_6 (reflectivity):

$$N_t = \frac{1}{\Delta t} \sum_{i=1}^{32} \frac{1}{A_i} \sum_{j=1}^{32} \frac{c_{ij}}{v_j}\,, \tag{3.3}$$

$$R = \frac{\pi}{6} \frac{1}{\Delta t} \sum_{i=1}^{32} \frac{D_i^3}{A_i} \sum_{j=1}^{32} c_{ij}\,, \tag{3.4}$$

$$M_1 = \frac{1}{\Delta t} \sum_{i=1}^{32} \frac{D_i}{A_i} \sum_{j=1}^{32} \frac{c_{ij}}{v_j}\,, \tag{3.5}$$

$$M_2 = \frac{1}{\Delta t} \sum_{i=1}^{32} \frac{D_i^2}{A_i} \sum_{j=1}^{32} \frac{c_{ij}}{v_j}\,, \tag{3.6}$$

$$M_6 = \frac{1}{\Delta t} \sum_{i=1}^{32} \frac{D_i^6}{A_i} \sum_{j=1}^{32} \frac{c_{ij}}{v_j}\,. \tag{3.7}$$

With Equations 2.7 and 2.13 the parameters of the gamma distribution N_0, μ, λ as well as D_0 are calculated. As stated earlier the method of Handwerker and Straub (2011) is applied here. In the context of this method they point out the following inconsistency:
The definition of the moments in Equation 2.8 is done for a diameter range from 0 to ∞. But, as shown in subsection 3.2.2, the measuring range of the disdrometer is limited to

D_{min} = 0.25 mm and D_{max} = 25 mm. Following the argument of Handwerker and Straub (2011) the complete moments M_k are composed as follows:

$$M_{k,\text{complete}} = \int_0^{D_{\text{min}}} n(D) D^k \, \mathrm{d}D + \int_{D_{\text{min}}}^{D_{\text{max}}} n(D) D^k \, \mathrm{d}D + \int_{D_{\text{max}}}^{\infty} n(D) D^k \, \mathrm{d}D \,. \tag{3.8}$$

The fact that small drops with $D < 0.25$ mm as well as large particles with $D > 25$ mm are missing in the DSDs due to the limitation of the disdrometer is known as truncation effect, which leads to truncated moments. In order to approximate the complete moments $M_{i,\text{complete}}$ from the measured moments $M_{i,\text{meas}}$, Handwerker and Straub (2011) introduce the approximated moments:

$$M_{k,\text{approx}} = \frac{M_{k,\text{meas}}}{\gamma(\lambda D_{\text{max}}, \mu + k + 1) - \gamma(\lambda D_{\text{min}}, \mu + k + 1)} \,, \tag{3.9}$$

with the incomplete gamma function γ. The definition of the approximated moments relies on values for μ and λ. However, to calculate these two parameters one is reliant on the moments. To deal with this reciprocal relationship, an iterative approach is utilised: the calculated $M_{k,\text{approx}}$ becomes $M_{k,\text{meas}}$ for the next iteration. This continues until the relative variations of μ and λ of two consecutive steps drops under a threshold of 1%.
Before this method is applied, resulting improvements of the measured moments are assessed by looking at the denominator d in Equation 3.9. The frequency distribution of d done for the entire data-set has a mean at $\overline{d}$ = 0.996 with a standard deviation of std(d) = 0.016. Dividing $M_{i,\text{meas}}$ by values so close to one makes $M_{k,\text{approx}}$ almost equal to it, immediately dropping under the threshold value for further iterations. Thus, this method provides no significant improvements and is therefore not applied in this thesis.

3.4 Quality control

3.4.1 Data filtering methods

A one-minute DSD spectrum must meet two conditions to qualify as rain. First, the rain rate must be larger than 0.1 mm h^{-1} in order to reduce noise. Secondly, the total particle count of a sample needs a minimum of N = 100 hydrometeors. Smith and Kliche (2005) as well as Handwerker and Straub (2011) show that parameters describing DSDs deduced by the moments method have a decreasing bias with increasing sample size. As a reasonable minimum N = 100 is presented to keep the bias at a decent low. This suggested limit is adopted here. Samples that do not meet these two conditions are not considered.

The data set still has many erroneous values. There are border-effects briefly mentioned in section 3.3. Drops that fall through the margins of the light beam are only partially

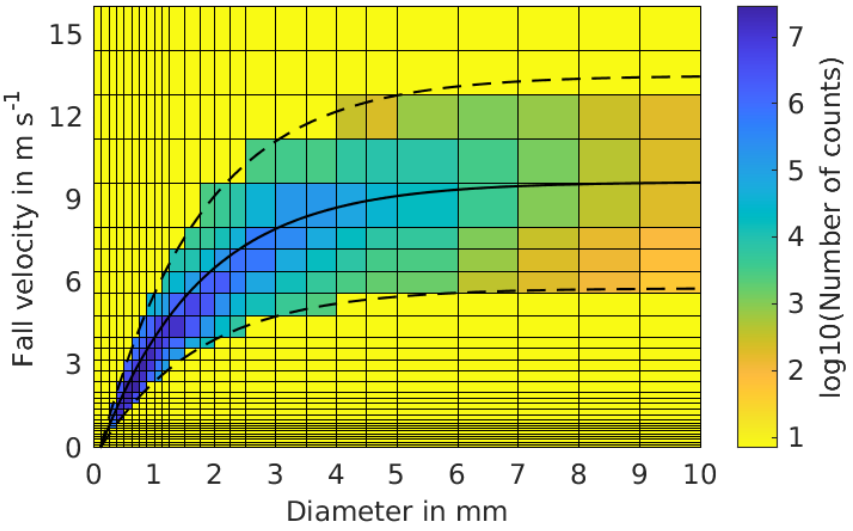

Figure 3.5: Scattergram of a DSD after filtering with the ±40% thresholds (dashed lines) in reference to the velocity-diameter relationship of Atlas et al. (1973) (solid line). Shown here is the data of the whole experiment period for all Parsivels. The grid lines represent the size and velocity bins in which the particles are classified.

registered by the disdrometer. This leads to a flawed size and fall velocity classification, resulting in the presence of smaller drops with higher fall velocities in the measured spectra than there actually are. Further possible reasons for erroneous measurements are strong winds, especially in combination with heavy rainfall. Friedrich et al. (2013a) who found this effect hypothesise that the reason for this are hydrometeors not moving perpendicular through the sampling area of the Parsivel. They observed an increased number of unrealistically large slow-falling drops in the erroneous spectra.
To address these measurement effects a filter is applied, which compares the observed velocity of drops $v_{obs}(D_i)$ to the terminal velocity of the mean particle size of the ith size bin $v_t(D_i)$, using the $v_t(D)$ relationship of Atlas et al. (1973) (Equation 2.3). This comparison is based on the assumption that the precipitation type measured is rain because the $v_t(D)$ relationship of Atlas et al. (1973) was determined for raindrops. Particles with $|v_{obs}(D_i) - v_t(D_i)| < 0.4 v_t(D_i)$ pass the filter, reducing hydrometeors to those that are within a ±40% threshold of the reference fall speed relation (Figure 3.5). Since the allowed absolute deviation from the reference fall speed increases with larger fall velocities, large hydrometeors such as hailstones are not discarded by the filter.
A previously tested threshold of ±60% was not utilised because many erroneous spectra were still present. The ±40% threshold is recommended by Kruger and Krajewski (2002) and in comparable Parsivel measurements used, e.g., by Liu et al. (2021).

To reduce erroneous data further, another layer of quality control is applied. The 6th moment M_6 is calculated before and after the filter described above is applied to a sample, providing $M_{6,bf}$ (before filter) and M_6 (after filter). Multiplying the logarithm of M_6 and $M_{6,bf}$ by 10 yields the radar reflectivity factors Z and Z_{bf} in the commonly used unit dB_Z. If these two reflectivity factors differ by more than 3 dB, the sample is discarded.

After filtering, a total amount of 1 118 836 one-minute spectra is available including all Parsivels over the whole measurement period. This corresponds to about 35.5 days of measured rain by 22 Parsivels. Keep in mind that dry periods are not regarded in this thesis.

3.4.2 Technical issues

Potential sources of error in the deduced quantities are not only issues with the measuring process of the Parsivel but also with its system stability. The Parsivel 2020C (Pc, Bettenhausen) did not record any data from August 20 to September 05, 2021, likely because of problems with the power supply. No event of special interest took place near Pc during this period. However, Pc might have missed some rainfall events, potentially affecting the total amount of rain measrued by Pc.

3.4.3 Comparison of the Parsivel disdrometers

In this section, the measured data of the different Parsivels are compared as a means of quality control. Additionally, some methods to evaluate the acquired data are introduced. Anticipating the findings of section 4.1, the data are divided into three precipitation regimes:

1. The **measure regime** includes the entire data set, which are **all events passing the quality control** mentioned in subsection 3.4.1.
2. The **rain regime** includes events with rain rates of $\mathbf{R > 2\,mm\,h^{-1}}$, with a total of 262 512 one-minute spectra (23.5% of the measuring regime). This regime mainly contains stratiform rain.
3. The **strong rain regime** includes all events with $\mathbf{R > 20\,mm\,h^{-1}}$ with a total of 11 198 one-minute spectra (1% of the measuring regime). This regime primarily corresponds to convective precipitation.

The following section only deals with the rain and the strong rain regimes. Events of small rain rates are not particularly interesting and produce artifacts as is shown in the next chapter.

As mentioned in subsection 3.1.2, there were four measuring sites with more than one Parsivel. In Nürtingen, Burladingen and Haigerloch two Parsivels were present. Rottenburg was equipped with three Parsivels. These sites enable a special comparison through equal weather conditions. When comparing the curves that display the median volume diameter D_0 over the rain rate R measured by the Parsivels neighbouring each other, the data corresponds rather well up to values of $R > 20\,\mathrm{mm\,h^{-1}}$ shown in Figure 3.6, where Parsivels from the same site share the same color. However, deviations are visible even below this value, as for example the Parsivels in Nürtingen display. Above $R = 20\,\mathrm{mm\,h^{-1}}$

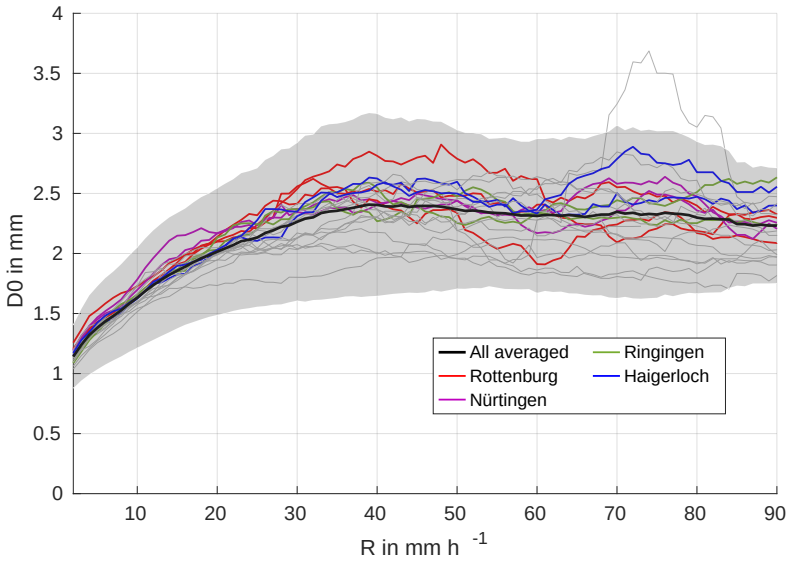

Figure 3.6: Median volume diameter over the rain rate determined for each Parsivel (grey lines). To avoid artifacts the values of D_0 are calculated with a moving average. The average range increases for higher rain rates, to compensate for the increased variability due to a decreasing number of events. In color are the lines at locations with more than one disdrometer. The black line shows the average over all devices with its standard deviation presented by the grey shaded area.

the data of collocated devices do not correspond well. Curves of equal color deviate heavily. This is especially true for very large rain rates. Events of large rain rates are rare, which is why individual events can influence the values associated with large rain rates strongly. An example for this is the only outlier that exceeds the standard deviation roughly between $R = 70$ and $R = 80\,\mathrm{mm\,h^{-1}}$ of the average of all devices (Figure 3.6). It is caused by a single hail fall event recorded by Ps in Großbettlingen on June 4, 2021.

To evaluate how well the data measured by two collocated disdrometers agree, a linear fit of the two-dimensional frequency distribution of the respective rain rates and median volume diameters is calculated. Additionally, the correlation coefficient ρ for these frequency distributions is determined (Table 3.2). According to Myers and Well (2003), the Pearson correlation coefficient is a measure of the extent to which two variables are linearly related and is defined as:

$$\rho(x, y) = \frac{1}{n-1} \sum_{i=1}^{n} \left(\frac{x_i - \overline{x}}{S_x} \right) \left(\frac{y_i - \overline{y}}{S_y} \right) , \tag{3.10}$$

with the standard deviation $S_x = \sqrt{\frac{1}{n-1} \sum_{i=1}^{n} (x_i - \overline{x})^2}$ and S_y likewise.

The Pearson correlation coefficient is prone to outliers in the data (Myers and Well, 2003). This issue is met by the filter methods (subsection 3.4.1) developed to reduce such outliers to a minimum. The interpretation of the correlation coefficient involves many difficulties (Myers and Well, 2003), but in this work it is used only to compare similar distributions and is therefore suited.

Curve fitting methods often use a least-squares approach, which determines the parameters of the fit function in such a way that the deviance of the data points to the function in y is minimized. Choosing to minimize the distance in y is problematic because it sets the parameter on the x-axis as an independent reference. However, none of the parameters compared in this work are known to be independent, which is why an orthogonal linear regression is used for all linear fits in this thesis (Adcock, 1878).

In general the data of two devices next to each other agrees well for measured rain rates as well as median volume diameters (exemplary locations in Figure 3.7). For larger rain rates and the corresponding median volume diameters the data corresponds less well (Figure 3.8). The question arises whether the spread comes from natural variations or from the measurement uncertainty of the device?

For two collocated disdrometers one would expect a correlation coefficient around one. There are three potential issues that could influence this result. One is the measurement error of the Parsivel. Another reason could be precipitation, that is not exactly identical for the two disdrometers. The third possible issue is of statistical nature, e.g., when many spectra with a small amount of particles occur. Quality control aims to eliminate such spectra to minimize this possible source of error.
To determine what natural variability can be expected, the investigation of Handwerker and Straub (2011) is consulted. They conducted a numerical experiment, where a random population of raindrops was constructed, obeying a predefined gamma-shaped DSD. This population was then sampled by an emulated disdrometer resulting in an idealised measurement. From this measurement they deduced an ideal standard deviation of D_0 depending on D_0, the shape parameter μ and the total number of drops given by the disdrometer N. This ideal standard deviation is now used to get an estimate for the natural variability of D_0 as it is measured by the Parsivels.
The data from the work of Handwerker and Straub (2011) mentioned above is still available. To transfer their findings for a predefined gamma-shaped DSD to actually measured DSDs of the data at hand, an interpolation is done. This interpolation is three-dimensional due to the dependency of deviation of D_0 on the above mentioned three parameters D_0, μ and N. Using a set of actually measured values of the three parameters as sampling points for the interpolation yields the standard deviation of D_0 as a function of the three parameters adjusted to the measured DSDs. Now a time series is constructed so that the parameters produce a spectrum of D_0 values that follows the just determined standard deviation. The last step is the multiplication of this spectrum, which emulates the measurement, by Gaussian noise creating natural variability. This is done twice to receive two independent spectra. Calculating the correlation coefficient of these two spectra gives an estimate of $\rho_{\mathrm{es}} = 0.98$ for the correlation coefficient, that results from the natural variability of the two spectra.

The correlation coefficients of the median volume diameter determined for collocated Parsivels range between $\rho_{D_0} = 0.96$ and 0.98 (Figure 3.7). The average correlation coefficient of the collocated disdrometers for the rain regime is $\overline{\rho_{D_0}} = 0.97$ and the average

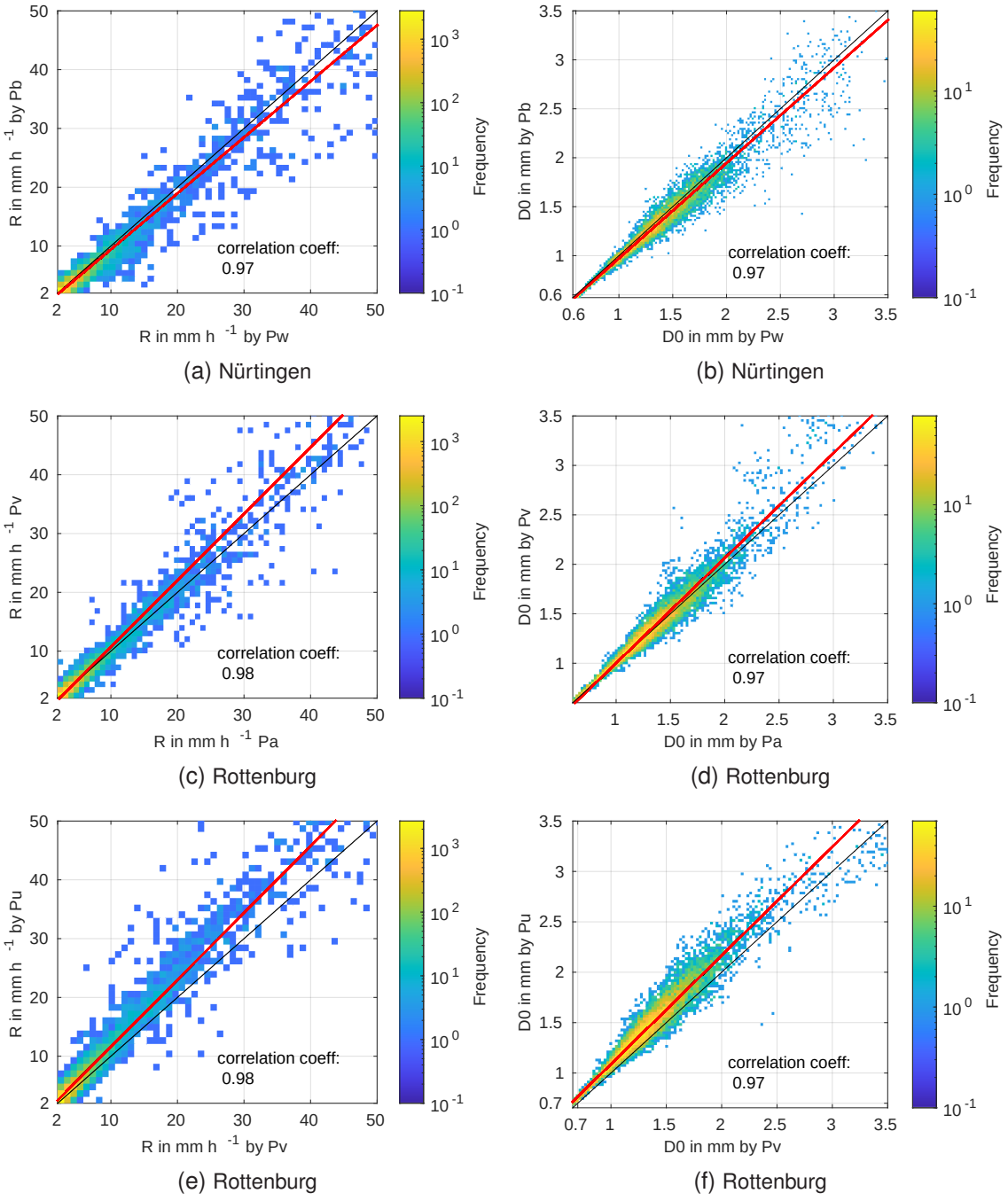

Figure 3.7: Comparison of measurements of collocated instruments in Nürtingen ((a),(b)) and Rottenburg ((c)-(f)) of the rain rate (left column) and median volume diameter (right column). The red line displays an orthogonal linear fit with $y = ax + b$. The respective values of the fit parameters a and b are stated in Table 3.2. The black line indicates a correlation coefficient of one for reference. The data used are of spectra with $R > 2\,\mathrm{mm\,h^{-1}}$.

Table 3.2: Correlation coefficients of measured R and D_0 of collocated Parsivels. Additionally, the fit parameters a and b of the respective orthogonal linear fits are stated (Figure 3.7,Figure 3.8). The first six lines present the rain regime and the bottom six the strong rain regime.

Collocated Parsivels	Location	ρ_R	a_R	b_R	ρ_{D_0}	a_{D_0}	b_{D_0}
Pw Pb	Nürtingen	0.97	1.0	-0.1	0.97	1.0	0.0
Pf Pe	Burladingen	0.98	0.9	0.4	0.97	0.9	0.1
Pt Pg	Haigerloch	0.96	0.9	0.0	0.96	1.0	0.0
Pa Pu	Rottenburg	0.99	1.3	-0.5	0.98	1.1	-0.1
Pv Pu	Rottenburg	0.98	1.1	0.2	0.97	1.1	0.0
Pa Pv	Rottenburg	0.98	1.1	-0.6	0.98	1.1	-0.1
Pw Pb	Nürtingen	0.92	0.9	0.8	0.95	1.1	-0.1
Pf Pe	Burladingen	0.92	0.8	3.8	0.94	1.0	-0.1
Pt Pg	Haigerloch	0.90	0.8	7.0	0.93	1.0	-0.1
Pa Pu	Rottenburg	0.96	1.3	-2.5	0.97	1.1	0.1
Pv Pu	Rottenburg	0.95	1.1	3.6	0.96	1.0	0.3
Pa Pv	Rottenburg	0.96	1.2	-4.9	0.96	1.1	-0.1

slope parameter of the orthogonal linear fits (Table 3.2) is $\overline{a_{D_0}}$ = 1.0 with an average y-intercept of $\overline{b_{D_0}}$ = 0.0. With the presented fit parameters in combination with an average correlation coefficient close to the estimate ρ_{es} = 0.98 determined above, it seems reasonable to assume that the observed variability of two collocated Parsivels is mainly due to the expected natural variability. The cause why the correlation coefficients deviate from one is likely a combination of all three issues stated in the passage above. All correlation coefficients for rain rate and median volume diameter for the rain and the strong rain regime of sites with multiple disdrometers are listed in Table 3.2.

Comparing the correlation coefficients and the fit parameters of the rain rate with those of the median volume diameter of the respective locations, small differences are observable (Table 3.2). One possible reason therefore might be small uncertainties that arise in the calculation of the parameters from the raw data (section 3.3). Another reason for the better agreement in the data of the median volume diameter compared to the rain rate might be the much larger value range of R compared to D_0.

Both rain rate and median volume diameter agree less well for events with higher rain rates presented by the strong rain regime (Figure 3.8), as indicated earlier at the discussion of Figure 3.6. The averaged correlation coefficients in this regime are ρ_R = 0.94 and ρ_{D_0} = 0.95, respectively. Here, the difference of the correlation coefficients of rain rate and median volume diameter at one location is larger than in the rain regime. This seems obvious considering the much reduced statistics of the rain regime. The coefficients of the

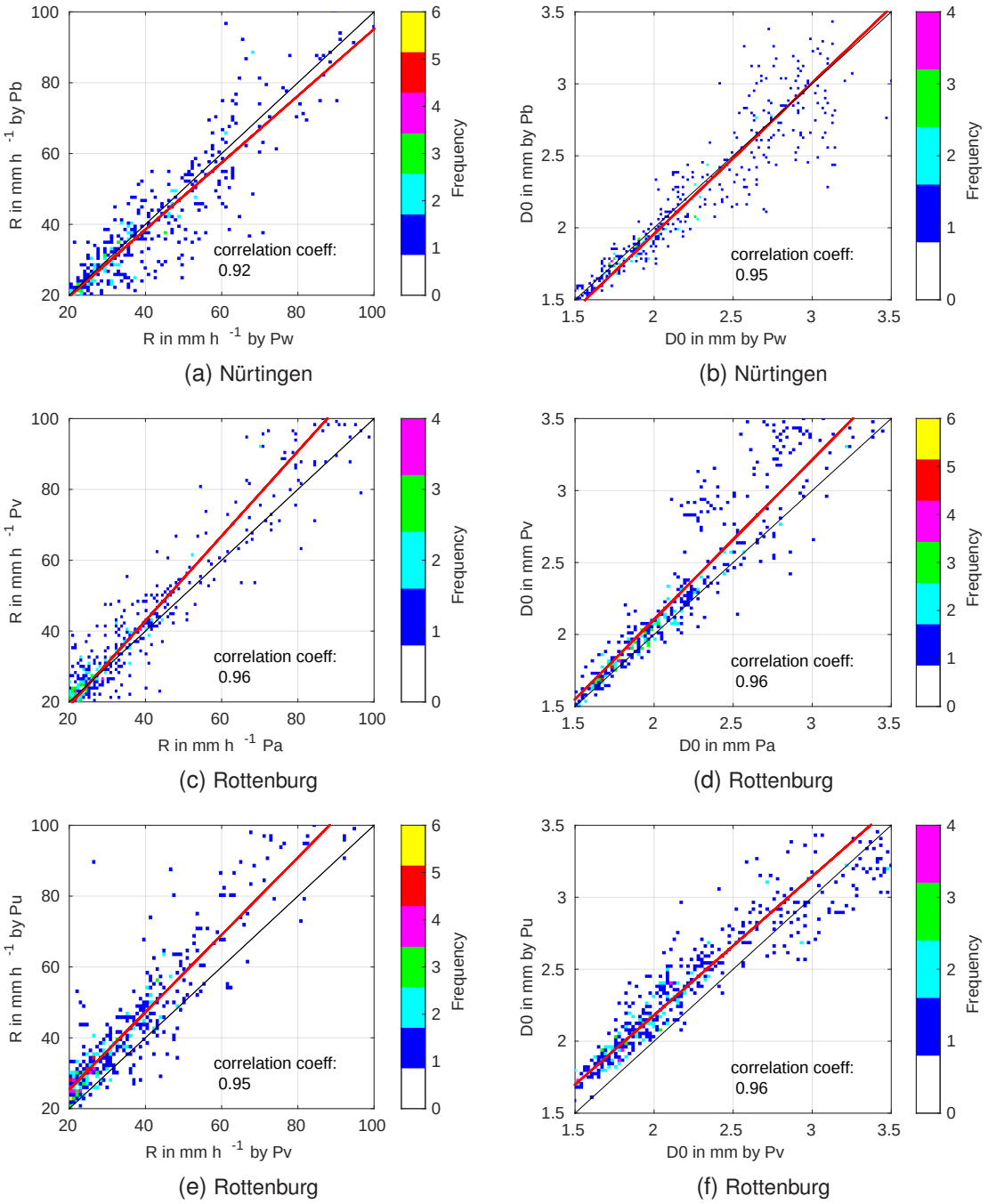

Figure 3.8: As in Figure 3.7 but for the strong rain regime. Due to the significantly smaller number of events in this regime, the color code is not logarithmic here.

median volume diameter are always higher or equal to those of the rain rate. This might be due to the reduced value range of the median volume diameter of events with high rain rates. However, the median volume diameter for this regime usually varies between about 2 and 2.4 mm, representing a much smaller value range.

The lowest correlation coefficients in both regimes are of the disdrometer pair Pt and Pg in Haigerloch. Also, the fit parameters of the rain rate in the strong rain regime of these Parsivels are striking due to the large offset of $b_R = 7$. Evaluating the data closer, it became clear that Pt measured some events of very high rain rates ($R > 100\,\mathrm{mm\,h^{-1}}$),

which Pg did not. This suggests that a strong rain occurrence has barely touched the location primarily hitting one of the devices, leading to this large offset. These individual strong rain events not causing entirely identical precipitation over two Parsivels at the same site might be the reason why the linear fits of the rain rates of the strong rain regime perform much worse than those of the rain regime.

An exception to the in general good agreements of collocated devices is Rottenburg, which becomes clear when looking at the linear fits of the Parsivels at that measring site (Figure 3.7). Parsivels of different age and device generation were set up here. As the name in Table 3.1 indicates, one of them was purchased in 2017, one in 2019 and one, as most other Parsivels, in 2020. The Parsivel Pu (2017) displays an anomalous measurement of rain rates. A systematic shift to higher rain rates in comparison to Pv (2019) is displayed in Figure 3.7e, also indicated by the y-intercept of the linear fit with $b = 0.2$. Comparing Pu with Pa exhibits the same behavior. That the fault lies with Pu is also emphasized by the well-agreeing data of Pv and Pa (Figure 3.7c,Figure 3.7d). The increased rain rates that Pu measures compared to the other two Parsivels at this location come from an increased drop count in the larger size classes of this Parsivel due to misclassification of drop sizes. Of course, this also affects the retrievals of the median volume diameter resulting in the shift toward Pu (Figure 3.7f). The shift of Pu in Rottenburg due to higher counts of big drops gets displayed even clearer in the strong rain regime (Figure 3.8e, Figure 3.8f). Connecting the misclassification of drop sizes of Pu to the age of this device, the aging laser diode seems one possible reason. However, the manufacturer OTT-HydroMet claims to consider the aging process of the laser diode in their retrieval algorithms. Results produced by Pu are not considered or, if they are, specifically mentioned in this thesis.

Although not systematically biased, the spread for rain events with $R > 20\,\mathrm{mm\,h^{-1}}$ is large for all locations; even more so for $R > 60\,\mathrm{mm\,h^{-1}}$. Regarding the small number of events with such large rain rates, it is difficult to draw conclusions about the measurement accuracy of the Parsivel.

The correlation coefficients of all Parsivels were calculated for the rain regime. As a plausibility check, the resulting 231 coefficients are plotted over the distance of the respective pair of Parsivels. In the case of stratiform rain a decreasing correlation coefficient with increasing distance between devices is to be expected. But despite the frequent convective precipitation, one expects a decreasing correlation coefficient for longer distances between devices, since even rain events with large temporal and spatial variability are more likely to affect nearby Parsivels than distant ones. This expectation holds true, as shown in Figure 3.9 for the rain rate and in Figure 3.10 for the median volume diameter, further supporting the good functioning of the Parsivel measuring network. The Parsivels located next to each other display the highest correlation coefficients as expected. To determine the relationship of the correlation with distance, an exponential fit is performed for the rain rate and the median volume diameter, respectively. This fit must include the point (0,1), since measurements at the exact same spot must theoretically agree. Choosing the

function $\exp(-d/c)$ with one fit parameter c to fit the data ensures this. The parameter d is the distance of the respective compared Parsivels. Minimizing the distance squares of data points to the fit function yields a fit parameter of $c = 11.6\,\text{km}$ for the rain rate (Figure 3.9), and $c = 26.8\,\text{km}$ for the median volume diameter (Figure 3.10). The typical correlation length c of the rain rate is roughly half of that of the median volume diameter, which might be due to the larger value range of the rain rate compared to the median volume diameter.

A measure of the quality of these fits is given by the goodness of fit R-squared. It describes how well the fit corresponds to the variation of the data. It takes values between 0 and 1 and is defined by the ratio of the residual sum of squares (SSE), and the total sum of squares (SST) Fahrmeir et al. (2022):

$$\text{R-squared} = 1 - \frac{SSE}{SST}\,, \tag{3.11}$$

with the numerator SSE and denominator SST defined as:

$$SSE = \sum_{i=1}^{n}(y_i - \widehat{y}_i)^2 \qquad \text{and} \qquad SST = \sum_{i=1}^{n}(y_i - \overline{y})^2\,. \tag{3.12}$$

The variable y_i denotes the ith value of the data set of size n, while $\widehat{y}_i$ denotes the corresponding fitted value. The mean of the data set is presented by $\overline{y}$.

Applying this on the fit of the correlation coefficients of the rain rates one obtains a goodness of fit R-squared = 0.43. For the fit regarding the correlation coefficients of the median volume diameter one obtains R-squared = 0.78, showing a better quality of fit. Hypothesising, the reason for this might again be the smaller available value range of the median volume diameter compared to the rain rate, allowing less variation in the data.

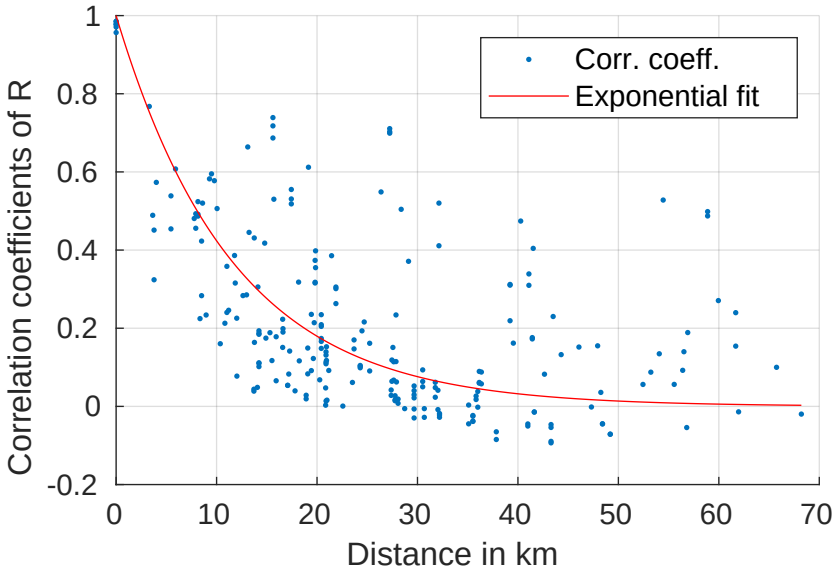

Figure 3.9: Correlation coefficients of all Parsivels with each other for R with a total of 231 data points plotted over the respective distance d of the pair. The correlation coefficients are calculated for the rain regime. The red line presents the exponential fit $\rho_R = \exp(-d/c)$ with $c \approx 12\,\text{km}$.

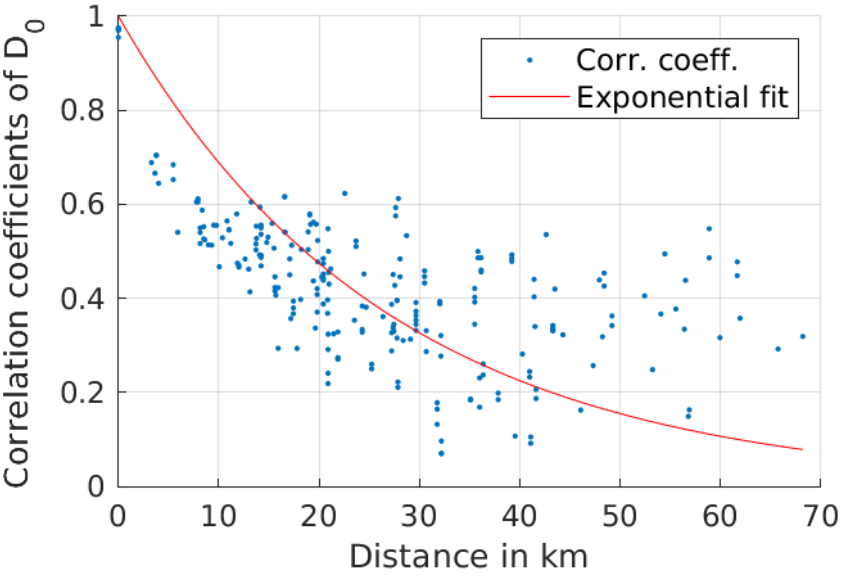

Figure 3.10: As in Figure 3.9 but for correltation coefficients of D_0. The exponential fit (red curve) $\rho_{D_0} = \exp(-d/c)$ has a fit parameter of $c \approx 27\,\text{km}$.

4 Results

4.1 Relations of gamma distribution parameters and the rain rate

Experience shows that the gamma distribution is a good, at least frequently used, approximation for measured DSD, especially for those measured with high temporal resolution. Mathematically, the gamma distribution has three parameters. However, previous work has shown that the gamma parameters are not independent (e.g. Testud et al. (2001); Liu et al. (2021)). By reformulating the analytical description, e.g., by normalizing with moments of the DSD, one searches for a description with independent parameters which then might describe independent physical properties of rain. These properties vary with the geographic and climatic regions, so it is useful to investigate our measurements in this regard.

To investigate the interdependency of the parameters of the gamma distribution for the data at hand as well as their relationship to the rain rate a set of two-dimensional frequency distributions is analysed (Figure 4.1). These distributions include the entire dataset, which means all Parsivels over the whole measuring time, above defined as measurement regime.
As commonly found (e.g. Handwerker and Straub (2011); Liu et al. (2021)), the frequency distribution of the shape parameter μ and the slope parameter λ displayed in Figure 4.1a exhibits a nearly linear dependency of the two parameters. Considering the relationship of μ and λ with D_0 (Equation 2.7), the linearity points to a rather constant median volume diameter. Lines of constant D_0 with the relationship $\mu = \lambda D_0 - 3.67$ from Equation 2.7 are drawn for comparison. Values of D_0 double with each isoline, with the smallest one presenting 0.1 mm and the largest presenting 6.4 mm. Evidently, a big amount of unexpected large values for both μ and λ are present in the distribution, creating a "tail" with a large spread. 95% of the respective μ and λ values are visible in the plot range. Also affected by these large values are the correlations between λ and D_0 and μ and D_0 depicted in Figure 4.1 (b), (c). Both of these plots also contain isolines of the respective parameter of Equation 2.7 not present in the frequency distribution. The μ isolines, which also double the value of μ with each step, present values of 1 up to 64. In Figure 4.1c, values for constant λ of 2 up to 64 mm^{-1} are plotted. The median volume diameter in relation to the rain rate shows a maximum ranging from 0.5 mm to 1.5 mm for rain rates mainly between 0.1 and 3 $\mathrm{mm\,h}^{-1}$ (Figure 4.1d).

Most samples refer to weak precipitation (Figure 4.1 (d), (e), (f)). These weak events produce artifacts in the form of the large values of μ and λ. If the rain rate is small, the probability for drops to be mainly in one size bin increases, which results in moments with $M_1^2 \approx M_0 M_2$. Calling back the premise of Equation 2.13, it becomes clear that this leads to unreliable values. In fact, 76.5% of all rain events of the data set have rain rates less than 2 mm h^{-1} raising the following question. Are the bright areas of Figure 4.1 that exhibit expected values for (a), (b) and (c) mere byproducts of the huge number of events with small rain rates, or do these bright maxima actually show a majority of the expected values across DSDs of all rain rates?

To prevent the bias of the large number of events with small rain rates, the frequency distributions are normalized (Figure 4.2). To do so, the sum over all events in one bin of a selected distribution is calculated. Here, the rain rate is chosen as normalizing distribution so that each bin is divided by the number of events of consant R. The two-dimensional frequency distribution of μ and λ shows a maximum at small expected values of both parameters after normalization, even though less clearly than before normalization (Figure 4.2a). A large spread of λ for small rain rates is particularly clearly displayed in Figure 4.2b. It also shows that events with larger rain rates produce rather constant values for λ, which is the expectation. Apart from the large spread present in the distribution of D_0 over R, a maximum that indicates an increasing median volume diameter with increasing rain rate can be seen (Figure 4.2c). This relation is further investigated later in this chapter.

The decrease of unexpected values of the gamma parameters for DSDs of increasing rain rates is exemplified in the $\mu - \lambda$ relation for different regimes of R (Figure 4.3). Not only do the large values decrease for increasing rain rates but the spread is also reduced. The axes range of Figure 4.3 (a) and (b) is different to (c) and (d), to make the smaller values of (c) and (d) well visible. However, the ratio of the axes stays constant making the slopes well comparable.

The large number of values with a big spread based on data of rain events with small rain rates and the decrease of unexpected values of events with higher rain rates led to the establishment of the three precipitation regimes "measurement", "rain", "strong rain", which were introduced in subsection 3.4.3.

A reduction of large values in all distributions concerning the gamma parameters is evident in the two-dimensional frequency distributions for the rain regime (Figure 4.4) compared to the measuring regime (Figure 4.1). All subfigures include 99% of the respective value range, which affirms the reduction of large values considering that Figure 4.1 and Figure 4.4 display the same value range. As already shown in Figure 4.3, the values in Figure 4.4a lost much of their "tail", while also narrowing the spread in the whole range. The maximum is now limited to values between approximately 4 and 5.5 for μ and 2.8 and 7.2 mm^{-1} for λ.

The maximum of the frequency distribution of λ over D_0 in the rain regime indicates an accumulation of events with median volume diameter values between 1.3 and 1.7 mm

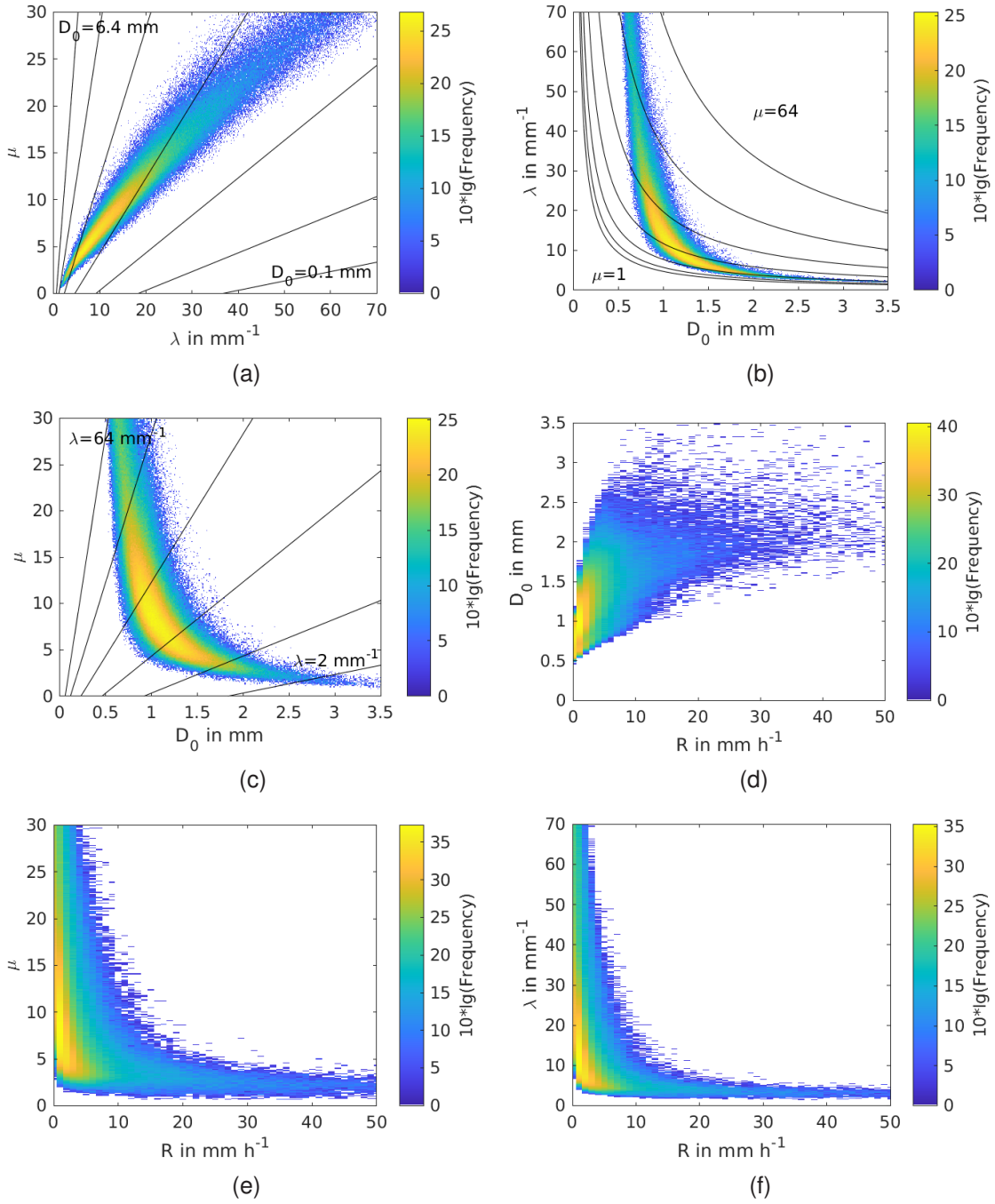

Figure 4.1: Two-dimensional frequency distributions on the base of the entire data-set for different parameters. In (a) μ and λ are displayed with the plot including 95% of their value range, respectively. (b) and (c) show these two parameters in their relation to D_0, again including 95% of value range of μ and λ but more than 99% of the range of values of D_0. μ, λ and D_0 are each individually plotted over R in (d), (e) and (f), including more than 99% of the value range of the rain rate.

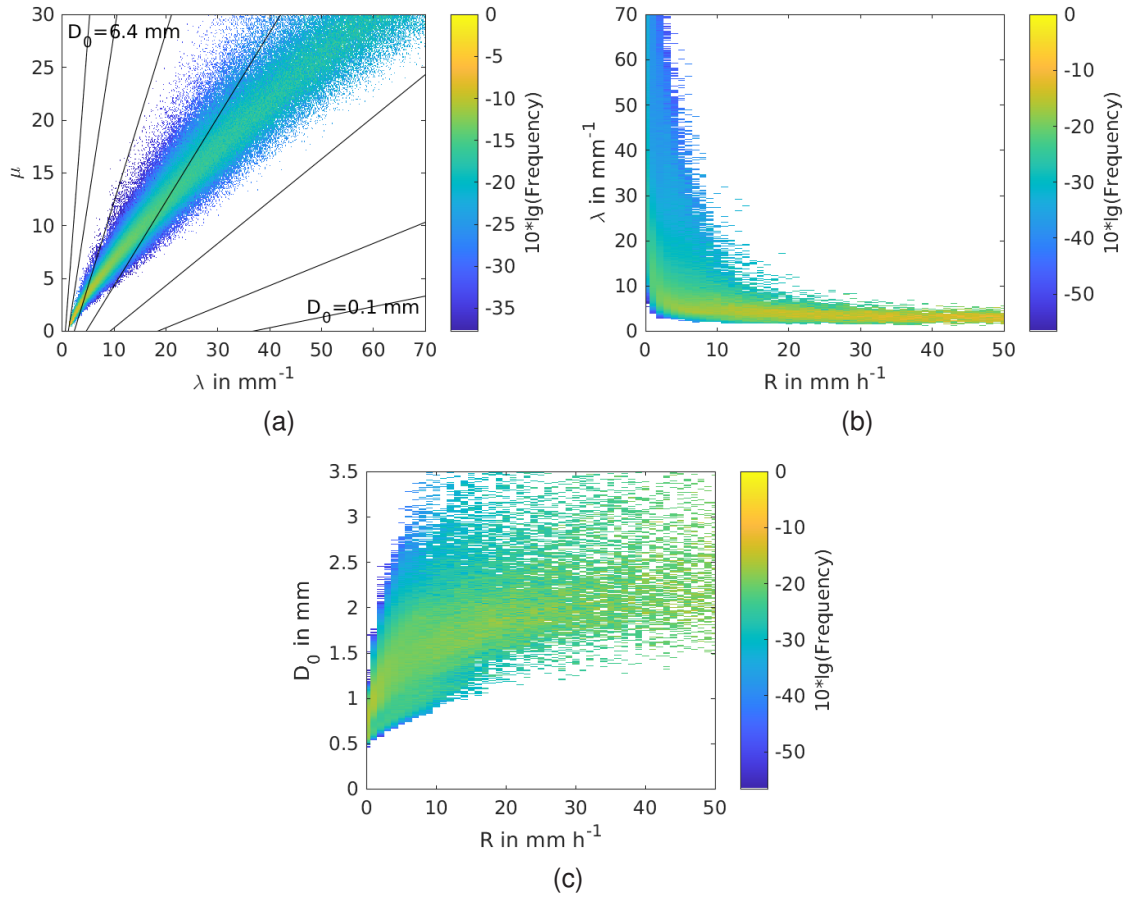

Figure 4.2: As Figure 4.1 (a), (d) and (f), but all bins of one distribution are normalized to the number of events of the respective other distribution in the very bin. Negative values on the colorbar are the consequence of normalization.

(Figure 4.4b). However, looking at the entire range the rain regime exhibits a relation of $\lambda \propto 1/D_0$ between the two parameters. In the two-dimensional frequency distribution of μ over D_0, the maximum covers a rather small range of μ values from about 4.2 to 5.2 (Figure 4.4c).

Though drastically reduced, nonphysical large values of λ for small rain rates are still not entirely extinguished as Figure 4.4d shows. Small rain rates tend to produce spectra with small median volume diameters (as was shown in Figure 4.2c). Therefore the large spread in μ and λ for small values of D_0 as discussed above, is likely also due to spectra of small rain rates.

As the parameters discussed before, the normalized intercept parameter N_L exhibits a large spread at small rain rates. It takes values, rather independent of the rain rate, ranging over about two and a half orders of magnitude with roughly $10^3 < N_L < 10^{5.5}$, indicating the necessity for a logarithmic scale (Figure 4.4e).
In chapter 2, the normalized intercept parameter was introduced to be only weakly dependent of μ. Figure 4.4f confirms this weak dependence.

The above anticipated relationship between median volume diameter and rain rate exhibits an increase of D_0 for increasing rain rates up to about $R = 40, \mathrm{mm\,h^{-1}}$ when a

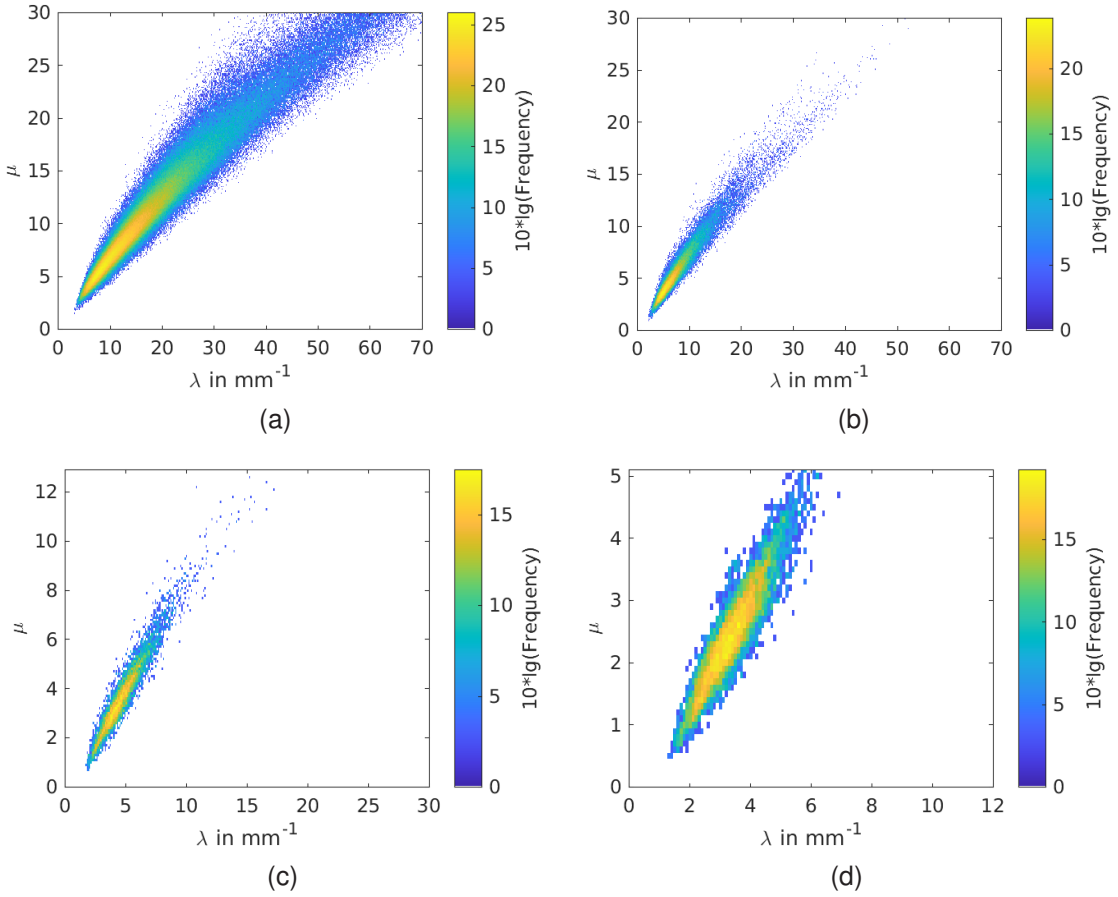

Figure 4.3: As in Figure 4.1a, but each Figure displays values deduced from a different set of rain events. The rain rates (in mm h^{-1}) displayed in each figure increase from (a) to (d) as follows: (a) $0.1 < R \leq 3$, (b) $3 < R \leq 10$, (c) $10 < R \leq 20$, (d) $R > 20$. In Figure 4.3c and Figure 4.3d a different axes range is chosen, but the ratio stayed the same.

maximum of D_0 = 2.4 mm is reached (Figure 3.6). This reflects what was previously indicated in Figure 4.2c. For increasing rain rates larger than R = 40, mm h^{-1}, the median volume diameter slightly decreases to about D_0 = 2.2 mm at R = 90, mm h^{-1}.

In the strong rain regime, the linear relation between μ and λ is displayed most clearly (Figure 4.5a). Values of λ range mainly between 2 and 5 mm^{-1} here. Values of μ primarily range between 1.5 and 4, providing no unexpected large values. Due to the strong range reduction compared to the other regimes, the axes range is adapted in all plots of Figure 4.5. An orthogonal linear regression of the two-dimensional frequency distribution of μ and λ yields a slope parameter of 0.9 mm^{-1} and an axis intercept of -0.7, with a goodness of fit R-squared = 93% (Figure 4.5a). This further confirms the linear relationship between the two parameters.

The values for λ over D_0 (Figure 4.5b) match well with the reference isoline of μ = 4. While the frequency distribution of μ and D_0 of the strong rain regime (Figure 4.5c) displays less interdependency of the two parameters than in the rain regime, it is still clearly noticeable. The good match of data and isoline in Figure 4.5b is therefore by chance. Values of μ range from about 1 to 5 in the strong rain regime while D_0 mainly ranges

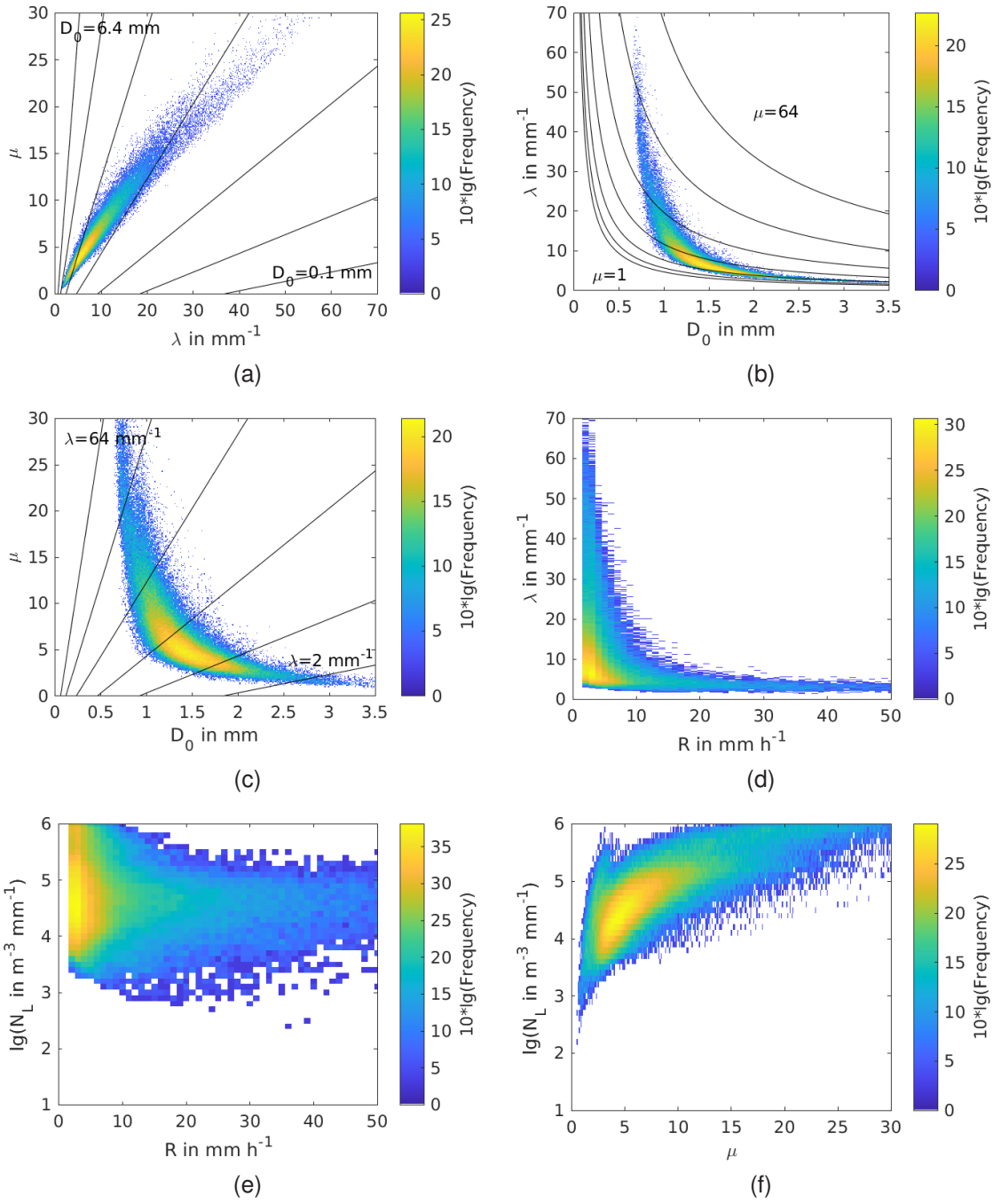

Figure 4.4: The subplots (a), (b) and (c) are as in Figure 4.1 but for the rain regime. (d) displays λ over R as in Figure 4.1f. (e) and (f) display the frequency distribution of the normalized intercept parameter N_L, which is presented in logarithmic scale. In all distributions 99% of the data is within the figures axes range.

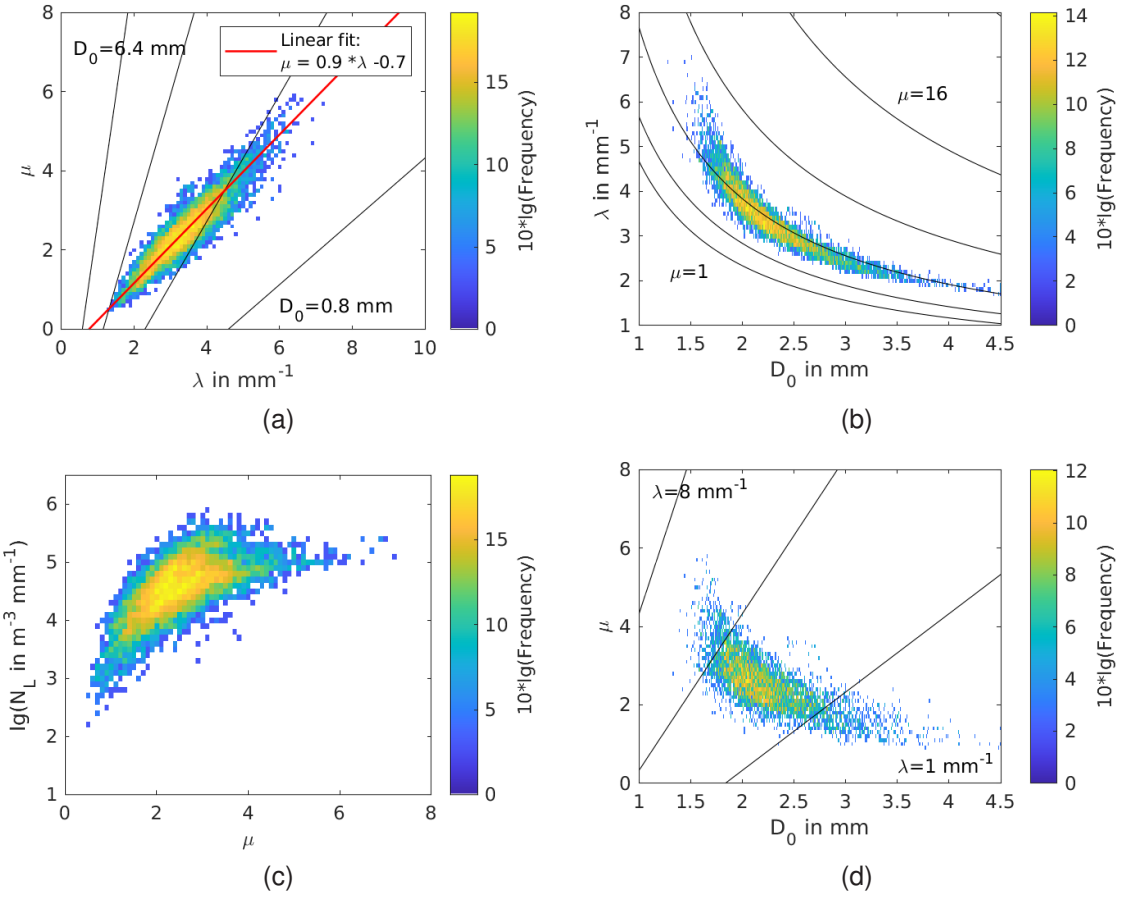

Figure 4.5: Two-dimensional frequency distributions for the strong rain regime. (a) displays the parameters μ and λ with the red line presenting a linear orthogonal fit. In (b) and (d) λ and μ over D_0 are shown, respectively. (c) displays lg(N_L) over μ.

between 1.6 and 3.5 mm.

Using data of the strong rain regime, the normalized intercept parameter N_L still ranges over more than two orders of magnitude (Figure 4.5d), similar to Figure 4.4f. The reduction of the value range of μ obviously affects the frequency distribution of N_L and μ, too. For the strong rain regime N_L still shows a slight dependence on μ. The maximum can be found at a rather constant value with $N_L \approx 5 \times 10^4\,\mathrm{m^{-3}\,mm^{-1}}$.

4.2 Spatial variability of DSD parameters

In order to get a characteristic DSD value for each measuring site, the median of the median volume diameter is calculated for each Parsivel with the data of the entire measuring period. This is done for the rain and the strong rain regime. Although rain rates smaller than $2\,\mathrm{mm\,h^{-1}}$ are excluded, the rain regime still exhibits some artifacts in the data set. These artifacts can have a strong influence on the mean value of the data, which is why the median is utilised here. In addition to the median volume diameter, the total amount of rain which each Parsivel respectively measured is calculated for both data regimes.

A difference between Parsivel measurements in the two different geographic areas Neckar Valley and Swabian Jura can be found for the median volume diameter as well as the total amount of rain. In the south-east of the measuring area the Swabian Jura is visible, with its ridge leading from south-west to north-east (Figure 4.6). The Parsivels therein, namely Pk, Pp, Pe, Pf, Pq, Pd and Ph (see Figure 3.1 for the locations) exhibit a slightly higher total rain amount than the ones in the Neckar Valley. Disdrometers Pk, Pp, Pe, Pf and Pq share an elevation of over 700 m MSL, while Pd and Ph are at 419 and 457 m MSL, respectively. This possibly indicates that the rain amount is influenced by the orographic features of this area rather than the altitude alone. However, much of the precipitation during the measurement campaign was convective and thus chance plays a large role. More data would be needed to confirm this observation. The size of the dots in Figure 4.6 displays the number of evaluated spectra, which is in general slightly larger for the sites in the Jura, implying more rain events there. The disdrometers in the Swabian Jura exhibit a distinctively smaller median of the median volume diameter compared to the devices in the Neckar Valley (Figure 4.7). The larger median volume diameters in the Neckar Valley might be due to the increased number of convective heavy rain events during the measurement period compared to the Swabian Jura. Hypothesising, orographically-induced precipitation in the hilly terrain of the Swabian Jura could be the reason for the additional rain events with rather small rain rates, resulting in the larger number of measured spectra in this area.

For the strong rain regime the differentiation between Neckar Valley and Swabian Jura becomes less clear. This is likely due to the more stochastic nature of convective events in this regime. An increased variability for this regime compared to the rain regime might also come from the strongly reduced number of measured spectra, providing a smaller statistic.
While Pk, Pd, Pp and Ph in the Swabian Jura (presented by the light blue dots) share a similar small total rain amount, Pq (presented by the orange dot) deviates heavily from them (Figure 4.8). The two collocated Parsivels furthest south, displayed by the green dot (Pe, Pf), also deviate from these three. The two Parsivels presented by the bright yellow dots (Po, Pl) exhibit the largest amount of rainfall in the strong rain regime. Located south of Tübingen, the disdrometer in Dußlingen (Pr) exhibits a significantly smaller number of measured spectra than all other sites. For the data of the rain regime (Figure 4.6) the same observation holds, implying a location with fewer rain events in comparison.
In the strong rain regime, the measured total amount of rain does not correlate with the median volume diameter. Two examples that show opposite behaviors are presented. First example are the disdrometers in Burladingen (Pe and Pf, green dot in Figure 4.8, furthest south) and the one in Hohenstein (Pq, orange dot, south-east). The two disdrometers in Burladingen measured less rain than the one in Hohenstein but their median of D_0 is larger. The second example are the disdrometers in the vicinity of Reutlingen (Pw, Pb, Po, Ps, Pl) and those in the Swabian Jura (Pp, Pk, Pd). Here, the Parsivels near Reutlingen measure a larger total amount of rain than those in the Jura, while simultaneously exhibiting a larger median drop diameter.

Overall, the stochastic nature of convective rain in the strong rain regime, causes large variations and makes it difficult to deduce general trends.

As mentioned above, the measurements of the Parsivel Pu deviates from the other disdrometers at the same site in Rottenburg. It generally classifies drops as too big, which is illustrated by the yellow rim of the dot west of Tübingen. In all four map plots (Figure 4.6 and following), Pu shows maximum values for both the total amount of rain and median volume diameter, further emphasizing its deviating measurements.

A detailed list of all gamma distribution parameters and the rain rate averaged over the whole measuring period for each Parsivel is provided in Table A.1 and following for the rain and the strong rain regime.

Assumptions about the general dependence of the median parameters on the elevation of its respective measuring site could not be validated, neither for the rain regime nor for the strong rain regime.

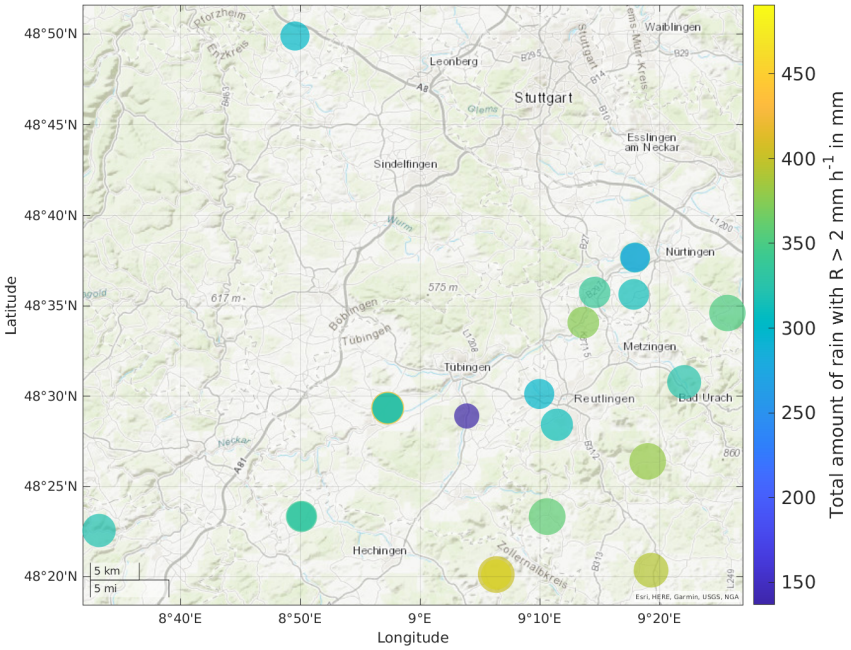

Figure 4.6: All measuring sites of the disdrometer network are shown here. The size of the dots present the number of measured spectra. The total amount of rain is indicated by the color code using the data of the rain regime. A topographic base map shows the orographic features of the area as well as its infrastructure.

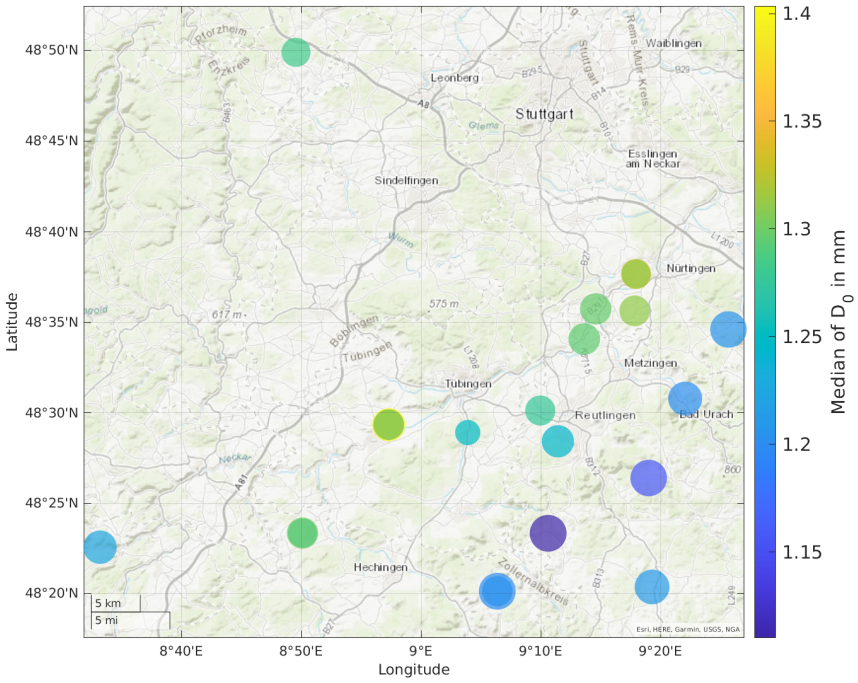

Figure 4.7: As in Figure 4.6 but here the color code displays the median of the median volume diameter.

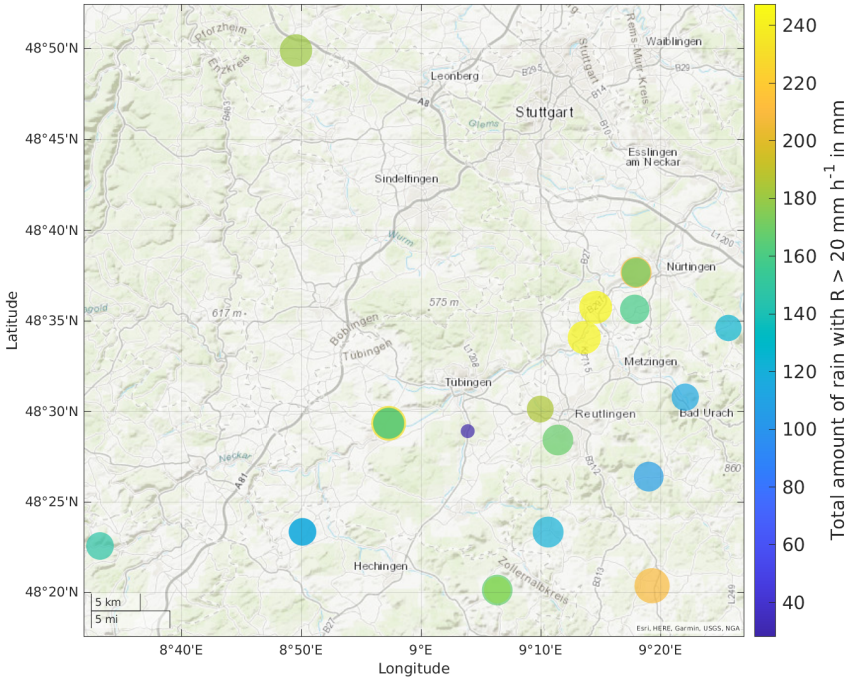

Figure 4.8: As in Figure 4.6 but for the strong rain regime. The dot size again exhibits the number of measured spectra. However, a different scale is used than in Figure 4.6 so that dot sizes are not comparable with those of the rain regime.

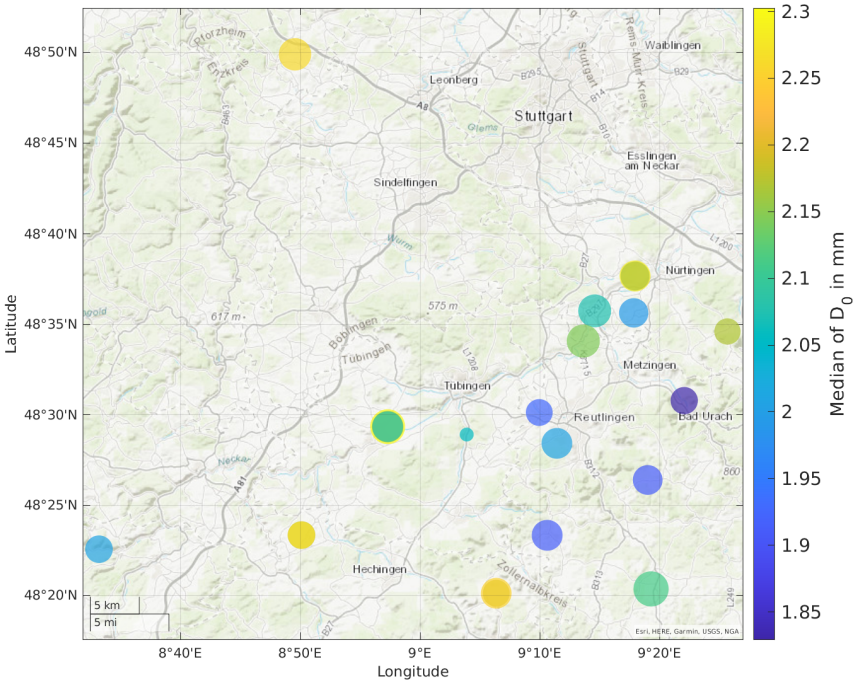

Figure 4.9: As in Figure 4.8 but the color code presents the median of the median volume diameter.

4.3 Case study of the supercell on June 23, 2021

On June 23, 2021 a supercell passed over the measuring area. Strong rain of up to 100 mm in less than an hour, heavy lightning activity and massive hailfall, leading to a layer of hail of up to 20 cm height in some areas, were some of its consequences. Massive damage to infrastructure and property was caused by flash floods and hail. The cell formed over Southern Black Forest around 13:30 UTC. It is the southernmost cell in Figure 4.10a. Figure 4.10 shows Max-CAPPI (Constant Altitude Plan Position Indicator) pictures, presenting the horizontal and vertical projection of maximum reflectivity recorded by the X-band radar of the KITcube, located in Nürtingen. The cell then moved along the Neckar Valley and the slopes of the Swabian Jura to the north-east (Figure 4.10) until it subsided near Schwäbisch Gmünd around 20:30 UTC.

By plotting a time series of the rain rate and the median volume diameter of the Parsivels affected by this event, the temporal and spatial variability of these two parameters can be assessed (Figure 4.11, Figure 4.12). As expected, the trajectory of the cell as recorded by the radar (Figure 4.10) perfectly matches the time and order in which the Parsivels recorded the first rain. Light rain from this cell was first recorded by the westernmost disdrometer Pc at 14:45 UTC, agreeing with Figure 4.10b. Next in line were Pt and Pg at Haigerloch already reaching rain rates of approximately 180 mm h^{-1}. At 15:40 UTC the thunderstorm hit the main measuring site in Rottenburg (Pv, Pa) with a maximum rain rate of 190 mm h^{-1}. Over Rottenburg the rain rate increased and decreased three times

within a short period with the third peak describing the maximum (Figure 4.13a). East of Rottenburg, the disdrometer Pr measured rain activity next. In comparison, it recorded only small rain rates. Since the cell center moved north-east, Pr only recorded the edges of the system. This is emphasised by the small median volume diameters measured at this site (Figure 4.12). Parsivel Pn, which was located east of Pr, barely showed any rain activity because it was even further away of the storm track. Continuing in north-easterly direction, all Parsivels in the densly equipped area between Reutlingen and Nürtingen displayed rain activity in succession as one would expect from the radar data. Pw and Pb in Nürtingen displayed the latest measured activity agreeing with their position furthest north-east in the Neckar Valley. By far the highest rain rate was measured by Ps in Groß-bettlingen peaking at a value as high as 377 mm h^{-1}.
No such distinct peak is observable for the time series of the median volume diameter (Figure 4.12). Peaking rain rates only rarely correspond to peaking median volume diameters, which is addressed in detail below for the Rottenburg site.
The time series of the rain rate as well as the median volume diameter display a strong intra-event temporal variability. Most peaks in the two time series are rather narrow, reflecting the rapid rates of change of the two rain properties R and D_0 in this thunderstorm.

As mentioned above, the temporal variability of R and D_0 do not peak or dip at the same time, as can be clearly seen when the cell was over Rottenburg (Figure 4.13). On the contrary, D_0 shows maxima around 15:43 and 16:10 UTC with values of approximately 3.7 mm, while the rain rate displays its highest peak at over 150 mm h^{-1} around 15:57 UTC. This agrees well with Schuur et al. (2001), who found that the median volume diameter takes on the largest values before and after the heaviest rainfall, associated with the passing of the convective core of a cell.
For the mostly stratiform rain of the rain regime, the median volume diameter was shown to increase for larger rain rates (Figure 3.6). This behavior, however, is totally different from the heavy convective rain shown here.

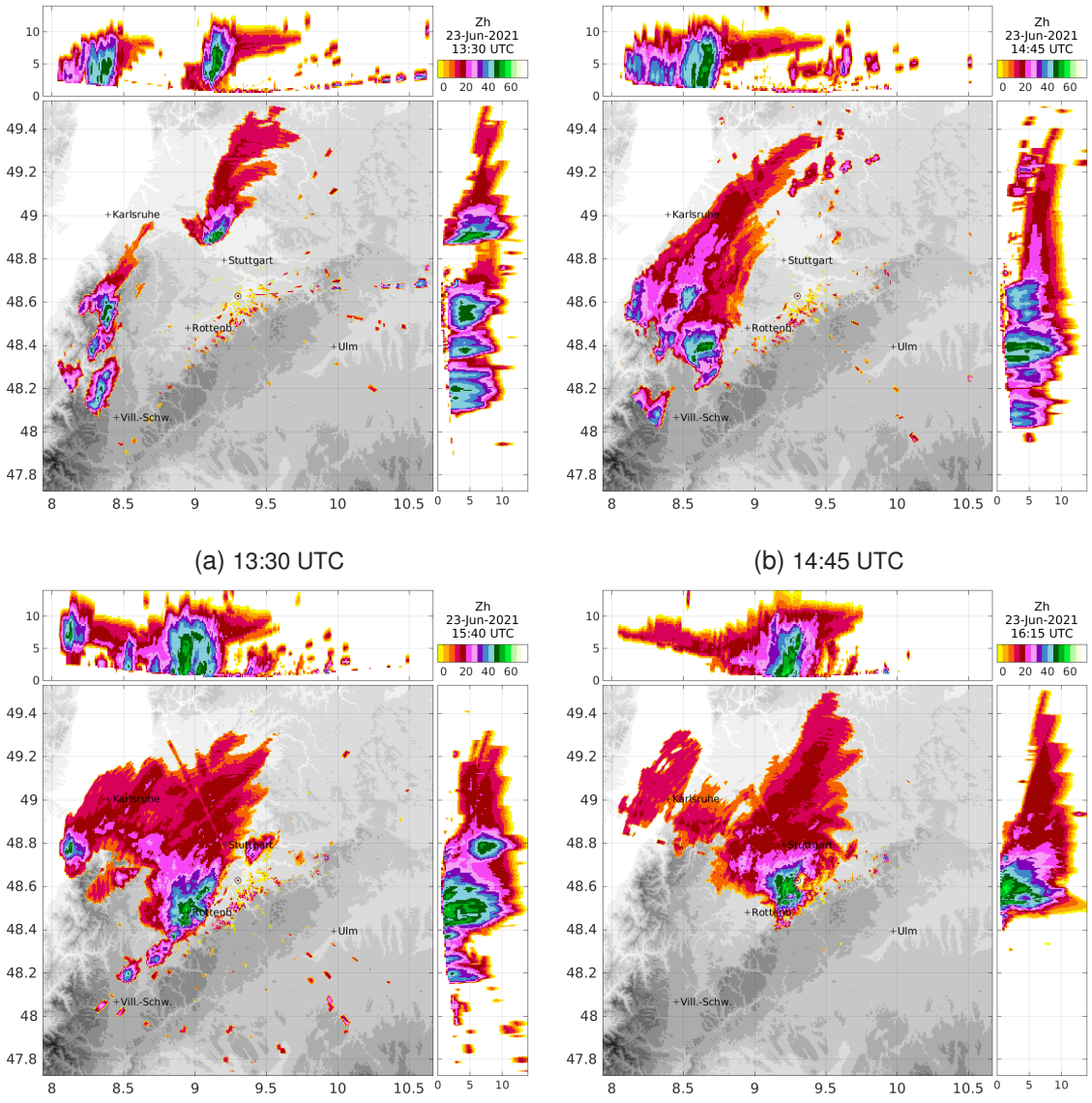

(a) 13:30 UTC

(b) 14:45 UTC

(c) 15:40 UTC

(d) 16:15 UTC

Figure 4.10: Max-CAPPI of the X-band radar located in Nürtingen, displaying the supercell moving along the Neckar Valley from south-west to north-east. If there is precipitation over the radar, then the radar signal is attenuated mainly by drops adhering on the radome. This results in a less reliable Max-CAPPI , when the cell reaches the radar. Additionally, the radar can only scan up to a certain azimuthal angle, which prevents it from seeing what is directly above. It seems as if the system shrinks in (c) and (d), which is an effect of these limitations. However, the center of the cell in green is well visible in all subfigures. The points in time were chosen in accordance to the events of interest in Figure 4.11.

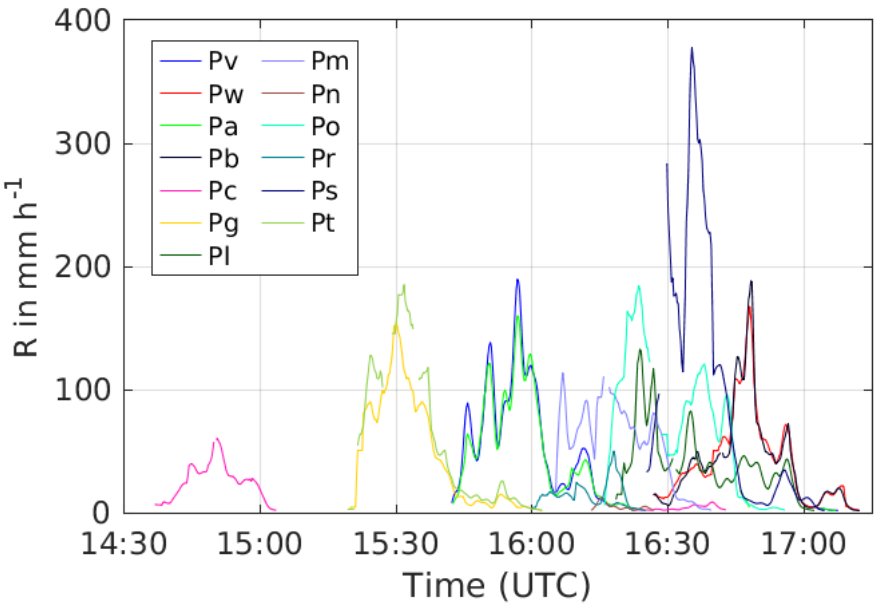

Figure 4.11: Time series of the rain rate for the Parsivels along the track of the supercell on June 23, 2021. The one minute measuring interval is converted to a 5 minute interval to smooth the curves. Parsivel Pu is not included here due to its erroneous measurements.

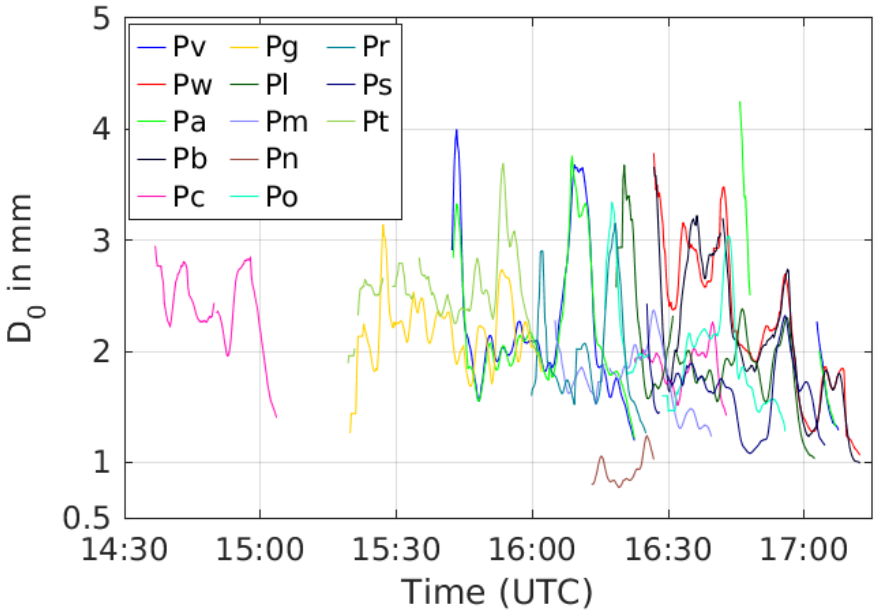

Figure 4.12: Same as Figure 4.11, but for the median volume diameter D_0.

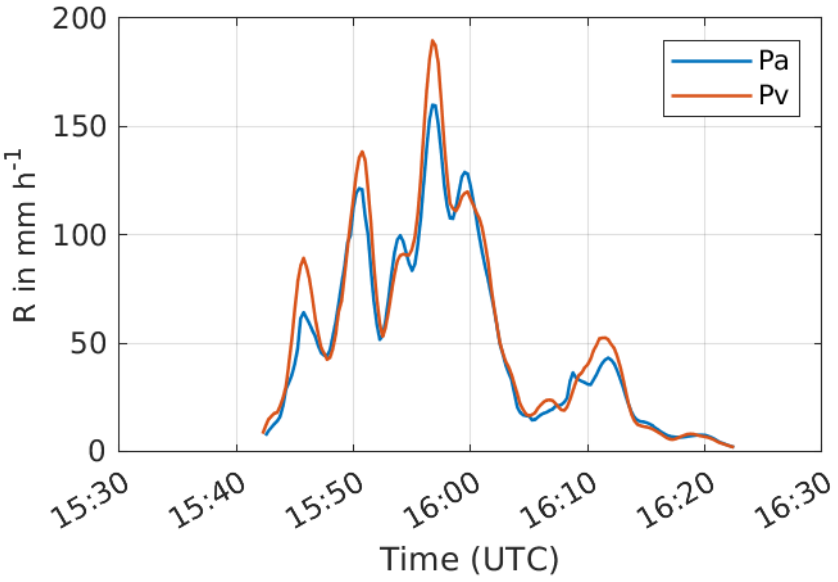

(a)

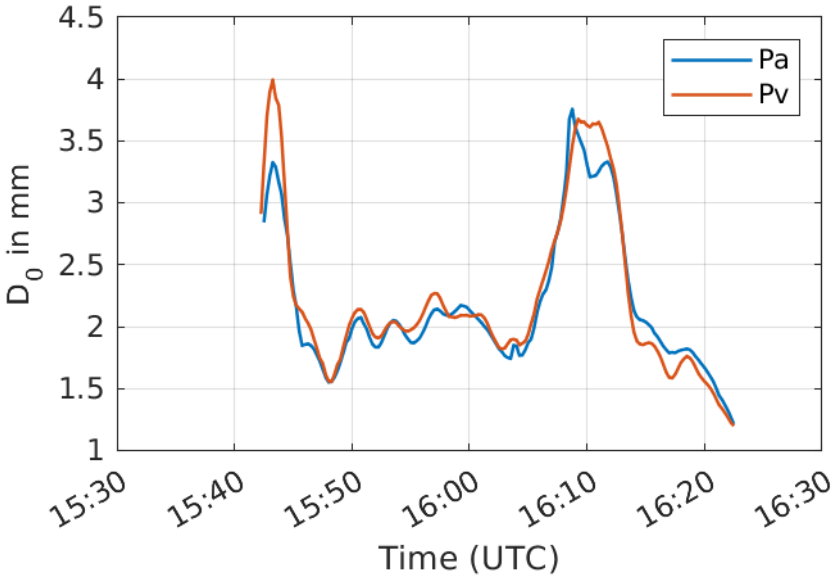

(b)

Figure 4.13: Same as Figure 4.11 and Figure 4.12, but for the main measuring site in Rottenburg (Pv, Pa).

5 Summary and conclusion

In this thesis we investigated DSDs and other precipitation properties of rain events from mid-April to October 8, 2021 in the Neckar Valley and the Swabian Jura. To describe the DSDs the gamma distribution was utilised. Its parameters were determined using the moments method. In the framework of the Swabian MOSES field campaign, the data was recorded by a network of 23 Parsivel disdrometers, which is part of the KITcube observation system. The analysis of the data also allowed an evaluation of the measuring network, which was fully deployed for the first time.

Four measuring sites with collocated disdrometers enabled to examine the measuring accuracy of the Parsivels. The measured rain rates and median volume diameters of close-by Parsivels were found to agree well. This was tested by linear regressions of the respective parameter, showing slopes around one and approximately no offset. In addition, the correlation coefficients of the median volume diameter of collocated disdrometers were compared with an estimated correlation coefficient resulting from the natural variability of this parameter (Handwerker and Straub (2011)), and they were found to be only slightly smaller. Thus, the deviation of the correlation coefficients from one is mainly due to natural variability. This is further confirmation of the consistent measurements of the Parsivels. However, for large rain rates the agreement of collocated Parsivels is significantly smaller. This is likely due to the more stochastic nature of convective precipitation, causing such large rain rates. High temporal and spatial variability leads to deviating conditions even for close-by devices. Yet another contributor to the decreased agreement of measurements of heavy rain might be the strongly reduced statistic of strong rain events due to their rare occurrence.
The correlation coefficients of all Parsivel pairs were determined. Investigating the behaviour of these coefficients with increasing distance of the respective disdrometer pair served as a plausibility check of the disdrometer network.
Concluding, the Parsivel network performs well. However, its performance in heavy rain conditions could profit from further assessment with more data available.
Through the direct comparison erroneous measurements of Parsivel PARS2017A were identified. It should be excluded in further studies.

A reduction in large artifacts of the determined gamma distribution parameters for spectra with larger rain rates was found by examining the frequency distributions thereof. This led to the definition of a rain regime with $R > 2\,\mathrm{mm\,h^{-1}}$ and a strong rain regime with $R > 20\,\mathrm{mm\,h^{-1}}$, which are further studied individually. These two data regimes also separate predominantly stratiform (rain regime) from convective (strong rain regime) rain.

Events with rain rates less than $2\,\mathrm{mm\,h^{-1}}$ were excluded in most examinations because gamma parameters reached nonphysical high values for these. Evaluation of the characteristics of gamma distribution parameters exhibited a nearly linear relationship of the shape parameter μ and the slope parameter λ, reproducing the findings of other studies (e.g. Chen et al. (2016); Liu et al. (2021)). This was supported by a median volume diameter D_0, whose means for events of large rain rates only vary over a small range of values. A median volume diameter increasing by about one millimeter with increasing rain rate was observed for $R < 40\,\mathrm{mm\,h^{-1}}$. Furthermore, the normalized intercept parameter N_L was found to be relatively constant for different rain rates. Knowledge on DSD parameters specific for the Swabian Jura and the Neckar Valley are essential for possible future advances in polarimetric radar products adapted for this region.
A limitation of the validity of the determined gamma distribution parameters comes from the influence the sampling time has on them. For example, spectra from long measuring intervals are well described by small values of μ. Therefore, it should be evaluated for future studies whether intervals other than one minute are more suitable for the deduction of DSD parameters. In this thesis one-minute spectra were used because they are most common in comparable research.

The measuring area can be divided into the regions Neckar Valley and Swabian Jura. The subdivision of these two regions is reflected by the distinguishable values of the total rain amount and the median volume diameter averages obtained for the rain regime for all Parsivels. In the Swabian Jura, one observes a tendency to higher rainfall totals and, surprisingly, smaller raindrop sizes, described by the median volume diameter D_0. At the same time, however, heavy precipitation events occur less frequently in the Jura. In the strong rain regime, the rainfall totals measured in the Swabian Jura are smaller than those measured in the Neckar Valley.

On June 23, 2021, a supercell moved through the measuring area causing massive damage to property and infrastructure in this region. By looking at the time series of the rain rate and the median volume diameter of the Parsivels that were in the vicinity of this cell, the temporal variability of these two parameters could be assessed. The trajectory of the cell as recorded by the X-band radar in Nürtingen perfectly matches the time when the Parsivels record rain. Focusing on the rainfall of this thunderstorm in Rottenburg, a strong temporal variability of DSD parameters in the strong rain regime becomes evident, even when examining 5-minute means. The largest values of median volume diameters are recorded before and after the heaviest rainfall associated with the convective core of this cell over Rottenburg, agreeing with observations of Schuur et al. (2001). This strong intra-event variability within very short time intervals presents a difficulty for comparisons between radar and in-situ DSD measurements in further studies.

The acquired assessment of the disdrometer network and the analysis of the data it collected is essential for further investigations concerning precipitation-related subjects. This includes quality control and improvements of radar observations and products, such as

the quantitative precipitation estimation (QPE), and research on microphysical processes of precipitation systems.

A Appendix

A.1

All gamma distribution parameters and the rain rate, averaged over the whole measuring period for each Parsivel, are listed here (Table A.1 and following). This is done for the data of the rain and strong rain domain. The averages stated are the mean and median, respectively. The median is the preferred average here because the mean is more susceptible to artifacts. Furthermore, the root-mean-square deviation σ of the median $\widetilde{P}$, with P being any parameter, is calculated as follows:

$$\sigma(P) = \sqrt{\frac{1}{N_{\text{tot}}} \sum_{m=1}^{N_{\text{tot}}} \left[P_m - \widetilde{P} \right]^2}. \tag{A.1}$$

For the intercept parameter N_0 the artifacts for some of the DSDs deviate over multiple orders of magnitude from the median, making a reasonable comparison impossible. For this reason, the parameter is not listed.

For the sake of completeness Parsivel Pu is also listed, despite its deviating measurments.

A.2

The Parsivel disdrometer classifies each measured drop in one of 32 size and 32 velocity classes. All drops within the interval of a certain class are assigned its mid-value. The precise class specifications are listed in Table A.7 and Table A.8 below.

Table A.1: DSD parameters (R, N_t, M_1) averaged over the measurement period for each Parsivel. The data used are the one-minute spectra of the rain domain ($R > 2\,\mathrm{mm\,h^{-1}}$). Of every parameter P, the mean $\bar{P}$, the median $\widetilde{P}$ and the root-mean-square deviation of the median $\sigma(P)$ is given. The minimum and maximum value of each column is marked in bold numbers.

Parsivel	R in $\mathrm{mm\,h^{-1}}$			N_t in $\mathrm{m^{-3}}$			M_1 in $\mathrm{mm\,m^{-3}}$		
	$\bar{R}$	$\widetilde{R}$	$\sigma(R)$	$\bar{N}_t$	$\widetilde{N_t}$	$\sigma(N_t)$	$\bar{M}_1$	$\widetilde{M_1}$	$\sigma(M_1)$
Pu	7.2	3.5	15.6	**465**	**318**	**460**	**407**	**285**	384
Pv	6.8	3.4	14.6	565	380	561	475	332	444
Pw	6.7	3.3	14.8	619	365	733	497	317	513
Pa	6.5	3.4	12.7	603	403	614	493	341	469
Pb	6.2	3.2	12.5	647	384	773	508	328	529
Pc	5.4	3.2	11.5	641	464	665	507	384	480
Pd	5.3	3.3	8.1	776	537	754	580	422	506
Pe	5.7	3.2	9.6	650	480	589	520	410	390
Pf	5.6	3.2	9.7	736	511	738	571	428	480
Pg	6.2	3.5	10.8	671	486	613	538	410	424
Ph	5.3	3.3	10.8	814	511	878	602	425	547
Pi	7.2	**3.9**	11.4	714	536	670	571	458	433
Pk	5.2	3.1	7.3	**931**	588	**1003**	**670**	468	601
Pl	7.1	3.3	15.9	652	409	722	527	354	525
Pm	6.5	3.3	16.4	645	412	744	528	356	**627**
Pn	6.0	3.2	11.8	719	453	772	557	381	547
Po	**7.5**	3.3	17.8	673	409	741	546	357	570
Pp	5.3	3.0	8.5	902	**606**	934	657	**479**	593
Pq	6.4	3.5	11.2	715	513	673	570	428	475
Pr	**4.1**	**2.9**	**4.7**	597	378	587	458	317	**378**
Ps	6.8	3.2	**18.6**	650	390	781	526	336	614
Pt	6.1	3.6	10.4	637	456	599	520	394	414

Table A.2: As in Table A.1 but for the parameters M_2, Z and μ.

Parsivel	M_2 in mm^2 m^{-3}			Z in dBZ			μ		
	$\bar{M}_2$	$\widetilde{M_2}$	$\sigma(M_2)$	$\bar{Z}$	$\widetilde{Z}$	$\sigma(Z)$	$\bar{\mu}$	$\widetilde{\mu}$	$\sigma(\mu)$
Pu	451	**308**	500	**34.9**	**33.8**	6.1	**4.8**	**4.0**	**3.3**
Pv	499	344	537	33.8	32.7	**6.0**	5.5	4.4	4.1
Pw	499	339	536	33.7	32.7	**6.0**	6.1	4.3	6.0
Pa	504	346	539	33.7	32.6	**6.0**	5.1	4.2	3.8
Pb	496	341	525	33.4	32.5	6.1	5.9	4.3	5.5
Pc	483	366	477	32.4	31.6	6.2	6.8	4.9	6.3
Pd	529	398	462	32.4	31.6	6.2	5.9	4.4	5.0
Pe	504	402	385	32.5	31.6	6.2	7.3	5.4	6.1
Pf	532	410	437	32.2	31.3	6.2	**7.8**	**5.7**	**6.7**
Pg	529	407	425	33.2	32.1	6.1	5.9	4.6	4.7
Ph	539	405	478	32.1	31.5	6.2	6.8	4.9	6.1
Pi	568	**449**	419	34.0	32.9	**6.0**	6.1	4.6	5.2
Pk	**579**	429	462	31.7	31.1	6.3	7.3	5.1	6.3
Pl	531	364	603	33.5	32.5	6.1	6.1	4.4	5.4
Pm	531	353	**768**	33.2	32.3	6.1	5.9	4.5	4.8
Pn	531	372	574	32.7	31.9	6.1	6.1	4.6	5.0
Po	554	368	685	33.6	32.6	**6.0**	5.9	4.3	5.0
Pp	571	434	504	**31.1**	**30.3**	**6.6**	7.6	5.6	6.2
Pq	554	415	480	33.1	32.0	6.1	6.5	5.0	5.4
Pr	**421**	316	**302**	32.1	31.7	6.2	5.8	4.5	4.2
Ps	525	342	687	33.4	32.5	6.1	5.8	4.3	5.0
Pt	518	399	404	33.5	32.8	6.0	6.1	4.7	4.8

Table A.3: As in Table A.1 but for the parameters λ, D_0 and N_L.

Parsivel	λ in mm^{-1}			D_0 in mm			N_L in 10^4 m^{-3} mm^{-1}		
	$\bar{\lambda}$	$\widetilde{\lambda}$	$\sigma(\lambda)$	$\bar{D_0}$	$\widetilde{D_0}$	$\sigma(D_0)$	$\bar{N_L}$	$\widetilde{N_L}$	$\sigma(N_L)$
Pu	**6.8**	**5.5**	**5.0**	**1.5**	**1.4**	0.5	**0.7**	**0.3**	**1.2**
Pv	7.8	6.2	6.3	1.4	1.3	0.5	0.9	0.4	1.5
Pw	8.9	6.0	9.9	1.4	1.3	0.5	1.2	0.4	2.6
Pa	7.6	6.0	6.0	1.4	1.3	0.4	1.0	0.5	1.7
Pb	8.8	6.1	9.2	1.4	1.3	0.4	1.3	0.4	2.7
Pc	9.8	7.0	9.2	1.3	1.2	0.4	1.2	0.6	2.0
Pd	9.2	6.7	8.1	**1.2**	1.2	0.3	1.4	0.7	2.4
Pe	10.5	7.4	9.5	1.3	1.2	0.4	1.3	0.6	2.2
Pf	11.3	7.8	**10.9**	1.3	1.2	0.4	1.6	0.7	2.7
Pg	8.7	6.6	7.4	1.3	1.3	0.4	1.2	0.6	2.0
Ph	10.5	7.2	10.3	1.3	1.2	0.4	1.8	0.6	3.2
Pi	9.0	6.5	8.4	1.4	1.3	0.5	1.3	0.6	2.4
Pk	11.4	7.7	10.8	**1.2**	1.2	0.4	**2.1**	**0.8**	**3.8**
Pl	8.9	6.2	8.7	1.4	1.3	0.4	1.2	0.5	2.4
Pm	8.6	6.5	7.6	1.3	1.3	0.4	1.1	0.5	1.9
Pn	9.2	6.7	8.3	1.3	1.2	0.4	1.4	0.5	2.4
Po	8.7	6.2	8.2	1.4	1.3	0.4	1.2	0.5	2.3
Pp	**11.8**	**8.5**	10.6	**1.2**	**1.1**	0.4	2.0	0.9	3.3
Pq	9.6	7.2	8.5	1.3	1.2	0.4	1.3	0.7	2.2
Pr	8.7	6.6	6.9	1.3	1.2	0.4	1.1	0.5	1.9
Ps	8.5	6.1	8.1	1.4	1.3	0.4	1.2	0.4	2.2
Pt	8.7	6.4	7.5	1.4	1.3	0.4	1.2	0.5	1.9

Table A.4: DSD parameters (R, N_t, M_1) averaged over the measurement period for each Parsivel. The data used are the one-minute spectra of the strong rain domain ($R > 20\,\mathrm{mm\,h^{-1}}$). Of every parameter P, the mean $\bar{P}$, the median $\widetilde{P}$ and the root-mean-square deviation of the median $\sigma(P)$ is given. The bold numbers mark the minimum and maximum value of each column.

Parsivel	R in $\mathrm{mm\,h^{-1}}$			N_t in $\mathrm{m^{-3}}$			M_1 in $\mathrm{mm\,m^{-3}}$		
	$\bar{R}$	$\widetilde{R}$	$\sigma(R)$	$\bar{N}_t$	$\widetilde{N_t}$	$\sigma(N_t)$	$\bar{M}_1$	$\widetilde{M_1}$	$\sigma(M_1)$
Pu	54.5	36.8	43.9	1049	**813**	810	1154	**903**	843
Pv	52.9	37.9	40.8	1286	928	1061	1347	1045	1014
Pw	53.3	39.4	40.6	1235	1072	837	1294	1072	875
Pa	48.1	35.4	33.8	1470	1114	1157	1459	1139	1065
Pb	48.1	37.4	32.9	1342	1054	1033	1338	1059	1000
Pc	46.9	32.9	44.4	1589	1060	**1832**	1451	1044	1514
Pd	38.4	29.3	24.9	1940	1640	1266	1656	1418	1058
Pe	42.7	33.2	25.6	1008	991	530	1095	1028	577
Pf	45.2	35.2	28.0	1056	890	905	1149	1021	895
Pg	43.5	32.2	29.8	1079	987	602	1119	1003	606
Ph	51.6	33.4	46.6	1348	1188	839	1400	1152	964
Pi	41.3	35.0	23.1	971	889	499	1005	937	455
Pk	35.5	29.4	17.2	1487	1258	952	1360	1199	774
Pl	56.0	37.6	45.0	1462	1267	878	1501	1250	943
Pm	**63.3**	43.4	**58.0**	**2156**	**1582**	1796	**2179**	**1481**	**1932**
Pn	47.1	36.0	32.5	1566	1226	1247	1550	1204	1224
Po	62.8	**44.0**	49.6	1548	1242	1170	1626	1227	1273
Pp	40.7	34.0	21.5	2008	1275	1803	1725	1169	1389
Pq	41.8	32.2	29.2	1275	1063	1064	1251	1049	924
Pr	**33.2**	**28.5**	**12.7**	**944**	1065	**429**	**997**	1097	**422**
Ps	61.0	36.9	68.1	1800	1242	1653	1806	1186	1671
Pt	44.4	33.2	32.8	981	936	561	1055	982	554

Table A.5: As in Table A.4 but for the parameters M_2, Z and μ.

Parsivel	M_2 in mm^2 m^{-3}			Z in dBZ			μ		
	$\bar{M}_2$	$\widetilde{M}_2$	$\sigma(M_2)$	$\bar{Z}$	$\widetilde{Z}$	$\sigma(Z)$	$\bar{\mu}$	$\widetilde{\mu}$	$\sigma(\mu)$
Pu	1798	1325	1284	51.9	51.6	5.8	1.6	1.5	0.9
Pv	1981	1485	1384	51.3	51.2	**5.7**	1.6	1.6	0.9
Pw	1911	1569	1236	52.4	52.5	6.0	1.5	**1.3**	1.0
Pa	2027	1509	1390	50.5	50.1	5.8	1.6	1.7	0.8
Pb	1876	1580	1245	51.8	51.6	5.8	**1.4**	**1.3**	0.9
Pc	1870	1412	1661	51.1	50.2	**5.7**	1.6	1.4	**1.3**
Pd	1991	1713	1214	**48.0**	47.6	**6.5**	1.7	1.5	1.1
Pe	1644	1444	857	50.3	49.8	5.8	1.7	1.7	0.9
Pf	1724	1466	1168	50.4	50.2	**5.7**	1.8	1.6	1.0
Pg	1639	1449	842	50.9	49.8	5.8	1.6	1.5	0.8
Ph	2029	1580	1502	50.4	49.3	5.9	1.7	1.5	1.2
Pi	1495	1403	598	50.0	49.8	5.8	1.6	1.4	1.0
Pk	1737	1557	849	**48.0**	**47.5**	**6.5**	1.8	1.5	1.1
Pl	2162	1680	1485	51.9	51.5	5.8	1.7	1.6	0.9
Pm	**2947**	1982	**2681**	50.9	50.5	**5.7**	**2.0**	**2.0**	0.8
Pn	2119	1641	1596	49.3	49.4	5.8	1.7	1.6	0.9
Po	2375	1745	1855	**52.5**	**52.6**	6.0	1.7	1.7	0.9
Pp	2075	1548	1383	48.7	48.2	6.2	1.6	1.5	**0.7**
Pq	1731	1471	1106	49.7	49.3	5.9	1.7	1.5	1.0
Pr	**1433**	1445	**522**	49.0	48.6	6.1	1.8	1.8	0.8
Ps	2436	1624	2147	52.3	50.9	**5.7**	1.9	1.8	1.1
Pt	1602	1432	805	50.6	49.3	5.9	1.6	1.6	0.8

Table A.6: As in Table A.4 but for the parameters λ, D_0 and N_L.

Parsivel	λ in mm^{-1}			D_0 in mm			N_L in 10^4 m^{-3} mm^{-1}		
	$\bar{\lambda}$	$\widetilde{\lambda}$	$\sigma(\lambda)$	$\bar{D}_0$	$\widetilde{D_0}$	$\sigma(D_0)$	$\bar{N}_L$	$\widetilde{N_L}$	$\sigma(N_L)$
Pu	**2.3**	2.3	0.9	**2.5**	**2.3**	0.8	**0.5**	**0.3**	0.5
Pv	2.5	2.4	1.0	2.4	2.2	0.8	0.7	0.4	0.8
Pw	2.4	**2.1**	1.1	2.4	**2.3**	0.6	0.7	0.4	0.7
Pa	2.6	2.5	0.9	2.3	2.1	0.8	0.8	0.5	0.8
Pb	2.4	2.3	1.0	2.3	2.2	0.7	0.7	0.4	0.9
Pc	2.7	2.6	**1.3**	2.2	2.0	0.8	1.1	0.5	**1.8**
Pd	**3.1**	2.9	1.2	**1.8**	**1.8**	**0.3**	1.2	0.8	1.1
Pe	2.5	2.5	0.9	2.3	2.2	0.6	**0.5**	0.4	0.4
Pf	2.5	2.4	0.9	2.4	**2.3**	0.6	0.6	0.4	0.7
Pg	2.5	2.4	**0.8**	2.3	2.2	0.6	**0.5**	0.5	0.4
Ph	2.6	2.4	1.2	2.2	2.2	0.6	0.7	0.6	0.7
Pi	2.4	2.2	1.0	2.4	**2.3**	0.6	**0.5**	0.4	0.4
Pk	2.9	2.7	1.1	2.0	1.9	0.5	0.9	0.6	0.9
Pl	2.6	2.6	**0.8**	2.2	2.1	0.6	0.8	0.7	0.6
Pm	3.0	**3.0**	**0.8**	2.0	1.9	0.4	**1.3**	**0.9**	1.2
Pn	2.7	2.6	1.0	2.2	2.0	0.6	0.9	0.6	0.9
Po	2.5	2.5	0.9	2.3	2.1	0.7	0.8	0.6	0.8
Pp	2.8	2.7	1.0	2.0	1.9	0.5	**1.3**	0.6	1.6
Pq	2.6	2.4	1.0	2.2	2.1	0.6	0.7	0.5	0.8
Pr	2.7	2.7	**0.8**	2.2	2.1	0.5	**0.5**	0.6	**0.3**
Ps	2.9	2.8	1.1	2.2	2.0	**0.9**	**1.3**	0.7	1.6
Pt	2.4	2.3	0.9	2.4	**2.3**	0.7	**0.5**	0.4	0.4

Table A.7: Drop size classes of the Parsivel taken from the manual of the Parsivel (OTT-HydroMet, 2022)

Class number	Mid-value of class in mm	Class spread in mm
1	0.062	0.125
2	0.187	0.125
3	0.312	0.125
4	0.437	0.125
5	0.562	0.125
6	0.687	0.125
7	0.812	0.125
8	0.937	0.125
9	1.062	0.125
10	1.187	0.125
11	1.375	0.250
12	1.625	0.250
13	1.875	0.250
14	2.125	0.250
15	2.375	0.250
16	2.750	0.500
17	3.250	0.500
18	3.750	0.500
19	4.250	0.500
20	4.750	0.500
21	5.500	1.000
22	6.500	1.000
23	7.500	1.000
24	8.500	1.000
25	9.500	1.000
26	11.000	2.000
27	13.000	2.000
28	15.000	2.000
29	17.000	2.000
30	19.000	2.000
31	21.500	3.000
32	24.500	3.000

Table A.8: Fall velocity classes of the Parsivel taken from the manual of the Parsivel (OTT-HydroMet, 2022)

Class number	Mid-value of class in $m\,s^{-1}$	Class spread in $m\,s^{-1}$
1	0.050	0.100
2	0.150	0.100
3	0.250	0.100
4	0.350	0.100
5	0.450	0.100
6	0.550	0.100
7	0.650	0.100
8	0.750	0.100
9	0.850	0.100
10	0.950	0.100
11	1.100	0.200
12	1.300	0.200
13	1.500	0.200
14	1.700	0.200
15	1.900	0.200
16	2.200	0.400
17	2.600	0.400
18	3.000	0.400
19	3.400	0.400
20	3.800	0.400
21	4.400	0.800
22	5.200	0.800
23	6.000	0.800
24	6.800	0.800
25	7.600	0.800
26	8.800	1.600
27	10.400	1.600
28	12.000	1.600
29	13.600	1.600
30	15.200	1.600
31	17.600	3.200
32	20.800	3.200

Bibliography

Adcock, R. J., 1878: A problem in least squares. *The Analyst*, **5 (2)**, 53–54, URL `http://www.jstor.org/stable/2635758`.

Adirosi, E., L. Baldini, and A. Tokay, 2020: Rainfall and dsd parameters comparison between micro rain radar, two-dimensional video and parsivel2 disdrometers, and s-band dual-polarization radar. *Journal of Atmospheric and Oceanic Technology*, **37 (4)**, 621 – 640.

Atlas, D., R. C. Srivastava, and R. S. Sekhon, 1973: Doppler radar characteristics of precipitation at vertical incidence. *Reviews of Geophysics*, **11 (1)**, 1–35.

Azevedo Coutinho, M., and P. Pereira Tomás, 1995: Characterization of raindrop size distributions at the vale formoso experimental erosion center. *CATENA*, **25 (1)**, 187–197.

Battaglia, A., E. Rustemeier, A. Tokay, U. Blahak, and C. Simmer, 2010: Parsivel snow observations: A critical assessment. *Journal of Atmospheric and Oceanic Technology*, **27 (2)**, 333 – 344.

Beard, K. V., D. B. Johnson, and D. Baumgardner, 1986: Aircraft observations of large raindrops in warm, shallow, convective clouds. *Geophysical Research Letters*, **13 (10)**, 991–994.

Brandes, E. A., G. Zhang, and J. Vivekanandan, 2004: Comparison of polarimetric radar drop size distribution retrieval algorithms. *Journal of Atmospheric and Oceanic Technology*, **21 (4)**, 584 – 598.

Cao, Q., and G. Zhang, 2009: Errors in estimating raindrop size distribution parameters employing disdrometer and simulated raindrop spectra. *Journal of Applied Meteorology and Climatology*, **48 (2)**, 406 – 425.

Chen, B., Z. Hu, L. Liu, and G. Zhang, 2017: Raindrop size distribution measurements at 4,500 m on the tibetan plateau during tipex iii. *Journal of Geophysical Research*, **122**.

Chen, B., J. Wang, and D. Gong, 2016: Raindrop size distribution in a midlatitude continental squall line measured by thies optical disdrometers over east china. *Journal of Applied Meteorology and Climatology*, **55**, 621–634.

Chen, B., J. Yang, R. Gao, K. Zhu, C. Zou, Y. Gong, and R. Zhang, 2020: Vertical variability of the raindrop size distribution in typhoons observed at the shenzhen 356-m meteorological tower. *Journal of the Atmospheric Sciences*, **77 (12)**, 4171 – 4187.

Conrick, R., J. P. Zagrodnik, and C. F. Mass, 2020: Dual-polarization radar retrievals of coastal pacific northwest raindrop size distribution parameters using random forest regression. *Journal of Atmospheric and Oceanic Technology*, **37 (2)**, 229 – 242.

Fahrmeir, L., T. Kneib, S. Lang, and B. D. Marx, 2022: *Regression : models, methods and applications*. Second edition ed., Springer, Berlin, Heidelberg.

Feingold, G., and Z. Levin, 1986: The lognormal fit to raindrop spectra from frontal convective clouds in israel. *Journal of Applied Meteorology and Climatology*, **25 (10)**, 1346 – 1363.

Fluck, E., M. Kunz, P. Geissbuehler, and S. Ritz, 2021: Radar-based assessment of hail frequency in europe. *Natural Hazards and Earth System Sciences*, **21**, 683–701.

Friedrich, K., S. Higgins, F. J. Masters, and C. R. Lopez, 2013a: Articulating and stationary parsivel disdrometer measurements in conditions with strong winds and heavy rainfall. *Journal of Atmospheric and Oceanic Technology*, **30 (9)**, 2063 – 2080.

Friedrich, K., E. A. Kalina, F. J. Masters, and C. R. Lopez, 2013b: Drop-size distributions in thunderstorms measured by optical disdrometers during vortex2. *Monthly Weather Review*, **141 (4)**, 1182 – 1203.

Goddard, J. W. F., S. M. Cherry, and V. N. Bringi, 1982: Comparison of dual-polarization radar measurements of rain with ground-based disdrometer measurements. *Journal of Applied Meteorology and Climatology*, **21 (2)**, 252 – 256.

Haddad, Z., D. Short, S. Durden, E. Im, S. Hensley, M. Grable, and R. Black, 1997: A new parametrization of the rain drop size distribution. *IEEE Transactions on Geoscience and Remote Sensing*, **35 (3)**, 532–539.

Handwerker, J., and W. Straub, 2011: Optimal determination of parameters for gamma-type drop size distributions based on moments. *Journal of Atmospheric and Oceanic Technology*, **28 (4)**, 513 – 529.

Illingworth, A. J., and T. Blackman, 1999: The need to normalize rsds based on the gamma rsd formulations and implications for interpreting polarimetric weather radar. *International Conference on Radar Meteorology, 29 th, Montreal, Canada*, 629–631.

Illingworth, A. J., and T. M. Blackman, 2002: The need to represent raindrop size spectra as normalized gamma distributions for the interpretation of polarization radar observations. *Journal of Applied Meteorology*, **41 (3)**, 286 – 297.

Jaffrain, J., and A. Berne, 2011: Experimental quantification of the sampling uncertainty associated with measurements from parsivel disdrometers. *Journal of Hydrometeorology*, **12 (3)**, 352 – 370.

Ji, L., H. Chen, L. Li, B. Chen, X. Xiao, M. Chen, and G. Zhang, 2019: Raindrop size distributions and rain characteristics observed by a parsivel disdrometer in beijing, northern china. *Remote Sensing*, **11**, 1479.

Kann, A., I. Meirold-Mautner, F. Schmid, G. Kirchengast, J. Fuchsberger, V. Meyer, L. Tüchler, and B. Bica, 2015: Evaluation of high-resolution precipitation analyses using a dense station network. *Hydrology and Earth System Sciences*, **19 (3)**, 1547–1559.

KIT, 2021: swabianmoses.de. URL `https://www.atmohub.kit.edu/105.php`, accessed: 14 April 2022.

Kliche, D. V., P. L. Smith, and R. W. Johnson, 2008: L-moment estimators as applied to gamma drop size distributions. *Journal of Applied Meteorology and Climatology*, **47 (12)**, 3117 – 3130.

Kruger, A., and W. F. Krajewski, 2002: Two-dimensional video disdrometer: A description. *Journal of Atmospheric and Oceanic Technology*, **19 (5)**, 602 – 617.

Liu, X., L. Xue, B. Chen, and Y. Zhang, 2021: Characteristics of raindrop size distributions in chongqing observed by a dense network of disdrometers. *Journal of Geophysical Research: Atmospheres*, **126 (24)**, e2021JD035 172.

Lopez, C., F. J. Masters, and K. Friedrich, 2011: Capture and characterization of wind-driven rain during tropical cyclones and supercell thunderstorms. *Proc. 13th Int. Conf. on Wind Engineering*.

Löffler-Mang, M., and U. Blahak, 2001: Estimation of the equivalent radar reflectivity factor from measured snow size spectra. *Journal of Applied Meteorology (1988-2005)*, **40 (4)**, 843–849.

Löffler-Mang, M., and J. Joss, 2000: An optical disdrometer for measuring size and velocity of hydrometeors. *Journal of Atmospheric and Oceanic Technology*, **17 (2)**, 130 – 139.

Mallet, C., and L. Barthes, 2009: Estimation of gamma raindrop size distribution parameters: Statistical fluctuations and estimation errors. *Journal of Atmospheric and Oceanic Technology*, **26 (8)**, 1572 – 1584.

Marshall, J. S., and W. M. K. Palmer, 1948: The distribution of raindrops with size. *Journal of Atmospheric Sciences*, **5 (4)**, 165 – 166.

Myers, J. L., and A. D. Well, 2003: *Research design and statistical analysis*. 2nd ed., Lawrence Erlbaum Associates, Mahwah, New Jersey.

OTT-HydroMet, 2022: *Operating instructions Present Weather Sensor OTT Parsivel²*. URL `https://www.ott.com/download/operating-instructions-present-weather-sensor-ott-parsivel2-without-screen-heating-1/`, accessed: 14 April 2022.

Pruppacher, H. R., and K. V. Beard, 1970: A wind tunnel investigation of the internal circulation and shape of water drops falling at terminal velocity in air. *Quarterly Journal of the Royal Meteorological Society*, **96 (408)**, 247–256.

Pruppacher, H. R., and J. D. Klett, 1997: *Microphysics of clouds and precipitation*. 2nd ed., Kluwer Acad. Publ., Dordrecht [u.a.].

Puskeiler, M., M. Kunz, and M. Schmidberger, 2016: Hail statistics for germany derived from single-polarization radar data. *Atmospheric Research*, **178-179**, 459–470.

Rogers, R. R., and M. K. Yau, 1996: *A short course in cloud physics*. 3rd ed., Butterworth Heinemann, [Woburn, Mass.].

Ryzhkov, A. V., 2019: *Radar Polarimetry for Weather Observations*. Springer, Cham.

Schmidberger, M., 2018: Hagelgefährdung und hagelrisiko in deutschland basierend auf einer kombination von radardaten und versicherungsdaten. Ph.D. thesis, Karlsruher Institut für Technologie (KIT).

Schuur, T. J., A. V. Ryzhkov, D. S. Zrnić, and M. Schönhuber, 2001: Drop size distributions measured by a 2d video disdrometer: Comparison with dual-polarization radar data. *Journal of Applied Meteorology*, **40 (6)**, 1019 – 1034.

Sekhon, R. S., and R. C. Srivastava, 1971: Doppler radar observations of drop-size distributions in a thunderstorm. *Journal of Atmospheric Sciences*, **28 (6)**, 983 – 994.

Smith, P. L., and D. V. Kliche, 2005: The bias in moment estimators for parameters of drop size distribution functions: Sampling from exponential distributions. *Journal of Applied Meteorology*, **44 (8)**, 1195 – 1205.

Testud, J., S. Oury, R. A. Black, P. Amayenc, and X. Dou, 2001: The concept of “normalized” distribution to describe raindrop spectra: A tool for cloud physics and cloud remote sensing. *Journal of Applied Meteorology*, **40 (6)**, 1118 – 1140.

Thompson, E. J., S. A. Rutledge, B. Dolan, and M. Thurai, 2015: Drop size distributions and radar observations of convective and stratiform rain over the equatorial indian and west pacific oceans. *Journal of the Atmospheric Sciences*, **72 (11)**, 4091 – 4125.

Tokay, A., P. G. Bashor, E. Habib, and T. Kasparis, 2008: Raindrop size distribution measurements in tropical cyclones. *Monthly Weather Review*, **136 (5)**, 1669 – 1685.

Tokay, A., D. A. Short, C. R. Williams, W. L. Ecklund, and K. S. Gage, 1999: Tropical rainfall associated with convective and stratiform clouds: Intercomparison of disdrometer and profiler measurements. *Journal of Applied Meteorology*, **38 (3)**, 302 – 320.

Torres, D. S., J. M. Porrà, and J.-D. Creutin, 1994: A general formulation for raindrop size distribution. *Journal of Applied Meteorology and Climatology*, **33 (12)**, 1494 – 1502.

Ulbrich, C. W., 1983: Natural variations in the analytical form of the raindrop size distribution. *Journal of Climate and Applied Meteorology*, **22 (10)**, 1764–1775.

Vivekanandan, J., G. Zhang, and E. Brandes, 2004: Polarimetric radar estimators based on a constrained gamma drop size distribution model. *Journal of Applied Meteorology*, **43 (2)**, 217 – 230.

Weber, U., and Coauthors, 2022: Moses: A novel observation system to monitor dynamic events across earth compartments. *Bulletin of the American Meteorological Society*, **103 (2)**, E339–E348.

Weckwerth, T. M., J. W. Wilson, M. Hagen, T. J. Emerson, J. O. Pinto, D. L. Rife, and L. Grebe, 2011: Radar climatology of the cops region. *Quarterly Journal of the Royal Meteorological Society*, **137 (S1)**, 31–41.

Willis, P. T., 1984: Functional fits to some observed drop size distributions and parameterization of rain. *Journal of Atmospheric Sciences*, **41 (9)**, 1648 – 1661.

Yuter, S. E., D. E. Kingsmill, L. B. Nance, and M. Löffler-Mang, 2006: Observations of precipitation size and fall speed characteristics within coexisting rain and wet snow. *Journal of Applied Meteorology and Climatology*, **45 (10)**, 1450 – 1464.

Acknowledgement

First of all, I would like to thank my supervisor Dr. Jan Handwerker for his great support, who always took time for feedback and new scientific suggestions. His always kind manner was particularly helpful.
I would like to thank my advisor Prof. Dr. Michael Kunz for his critical but valuable feedback, which showed me room for further improvements. I am also grateful to my second advisor Prof. Dr. Corinna Hoose, who helped to find the scientific direction.
I would like to thank the members of the working group Land Surfaces and Boundary Layer and the technical staff for the great experience I had during the measuring campaign. Everybody was very helpful and I learned a great deal of practical knowledge.
I also would like to express my deep gratitude to my fellow students and friends, especially Ralf, Felix and Pablo, without whose mental support this work would have been unthinkable.
Lastly, I want to thank my family for always supporting me throughout my studies.

Declaration of Authorship

Ich versichere wahrheitsgemäß, die Arbeit selbstständig verfasst, alle benutzten Hilfsmittel vollständig und genau angegeben und alles kenntlich gemacht zu haben, was aus Arbeiten anderer unverändert oder mit Abänderungen entnommen wurde sowie die Satzung des KIT zur Sicherung guter wissenschaftlicher Praxis in der jeweils gültigen Fassung beachtet zu haben.

Karlsruhe, 27.04.2022

Sören Bergmann